Universidade Coimbra
Faculdade Ciências e Tecnologia
Departamento de Física

Two new types of laser Doppler flowmeters

Prototypes validation

Rita Helena Pinto Oliveira Campos
Coimbra, 2011

Two new types of laser Doppler flowmeters

Prototypes validation

Rita Helena Pinto Oliveira Campos

A Thesis submitted for the degree of Integrated Master in Biomedical Engineering

Department of Physics
Faculty of Science and Technology, University of Coimbra

Coordinator:

Ph.D Requicha Ferreira

Supervisor:

M.Sc Edite Figueiras

September 2011

This work was supported by Fundação para a Ciência e a Tecnologia and by the European Social Fund through “Programa Operacional Factores de Competitividade (POFC)”, through the grants PTDC/SAU-BEB/101719/2008 and PTDC/SAU-NEU/101726/2008.

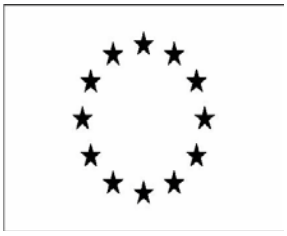

Acknowledgment

The work reported in this thesis was carried out at Group of Electronic and Instrumentation, in the Department of Physics of the Faculty of Sciences and Technology in University of Coimbra.

I would like to thank the elements of Group of Electronic and Instrumentation their availability and given support. Especially I wish to express my deepest gratitude to my supervisor Master Edite Figueiras for the help on the thesis and for all guidance, concern, and spend time during this year. I also want to thank my coordinator, Professor Requicha Ferreira, for the given opportunity and for reviewing this thesis.

In a special way I wish to thank my parents for the unconditional support, and to my closest friends for the pleasant time we spent together.

Abstract

Laser Doppler flowmetry (LDF) is a technique for real-time assessment of microcirculation blood flow. LDF can be used for non-invasive perfusion monitoring (e.g. skin perfusion monitoring), or for invasive microcirculation evaluations (e.g. perfusion brain evaluations). In this thesis, we aim to add depth discrimination capabilities to LDF skin monitoring using a multi-wavelength laser Doppler flowmeter prototype with different spaced detection fibres. We also aim to build a self-mixing based laser Doppler flowmeter prototype for brain perfusion estimation. In order to validate the two new prototypes, Monte Carlo simulations of light transport in tissue models were performed. For the non invasive prototype, simulations in a phantom (consisting of a moving fluid at six different depths) and in a skin model, were done. The results showed that the first moment of the photocurrent power spectrum (M1) and mean depth measured, both increase with emitting-receiving fibre distance. Moreover, we show that increasing the wavelength of incoming light increases the mean depth to be probed. For the invasive prototype validation, Monte Carlo simulations were carried out on a rat brain model. We show that the mean measurement depth in the rat brain with our probe is 0.15 mm. Measurements made with the non invasive prototype in the phantom and in the skin were compared with the Monte Carlo results. The measurements show quite good agreement with the simulations.

Resumo

A fluxometria laser Doppler (LDF) é uma técnica para avaliação em tempo real do fluxo microcirculatório em tecidos biológicos. Esta técnica pode ser usada para monitorização não invasiva da microcirculação (por exemplo, avaliação da perfusão na pele), ou para monitorização da perfusão de forma invasiva (por exemplo, avaliação da perfusão no cérebro).

Nesta tese, pretende-se acrescentar ao estado da arte da LDF, quando aplicada à monitorização não invasiva da perfusão na pele, a capacidade de discriminação em profundidade. Para isso, foi desenvolvido um protótipo de um fluxómetro laser Doppler com vários comprimentos de onda e diferentes separações entre as fibras emissora e receptora. Tendo em vista a monitorização de perfusão de cérebro de rato construiu-se um protótipo de um fluxómetro laser Doppler baseado na técnica self-mixing utilizando micro-fibras ópticas de forma invasiva.

Para validar estes dois novos protótipos, fizeram-se simulações Monte Carlo do transporte de luz em tecidos. Realizaram-se simulações num fantoma (constituído por seis camadas de fluido a diferentes profundidades), e num modelo da pele para a validação do protótipo não invasivo. Os resultados demonstraram que o primeiro momento do especto de potência (M1), assim como, a profundidade atingida pelos fotões, aumentam com o incremento da distância entre as fibras emissora e receptora. Para além disso, os resultados evidenciaram que o acréscimo do comprimento de onda da luz laser traduz-se numa maior profundidade média amostrada. Medições realizadas com o protótipo não invasivo no fantoma e na pele foram comparados com os resultados das simulações. As simulações aproximam-se bastante dos resultados das medições

Para a validação do protótipo invasivo, foram efectuadas simulações Monte Carlo num modelo de cérebro de rato. Foi demonstrado que a profundidade média medida com a sonda construída é de 0.15 mm..

Contents

Acknowledgment vii
Abstract IX
Resumo XI
Figures list XV
List of tables XVII
Abbreviations XIX
1- Introduction 1
1.1 Motivation 1
1.2 Purpose 2
1.3 Thesis structure 2
2- Laser Doppler Flowmetry 3
2.1 Introduction 3
2.2 Historical background 3
2.3 Medical background 3
2.3.1 Structure of the skin 3
2.3.2 Skin microcirculation 5
2.4 Theoretical analysis 6
2.4.1 Light source 6
2.4.2 Doppler shift and light interaction with the tissue 6
2.4.3 Doppler Power Spectrum 8
2.4.4 Measured variables 9
2.5 LDPM and LDPI 9
2.5.1 LDPM 10
2.5.2 LDPI 10
2.6 Applications 11
2.7 Technical limitations of LDF 12
2.7.1 Reproducibility of measurements 12
2.7.2 Absence of measurements units 12
2.7.3 Motion artifacts 12
2.7.4 Biological zero 12
3- Monte Carlo Method 13
3.1 Introduction 13

3.2 Fundamental optical properties: Absorption and Scattering 14
3.2.1 Absorption 14
3.2.3 Scattering 15
3.3 Software description 17
3.3.1 Simulation initialization 17
3.3.2 Light Sources 17
3.3.2 Algorithms applied to light transport in tissue 18
3.3.3 Detection 20
3.3.4 Specially Feature: Laser Doppler Flowmetry 21
3.4 Monte Carlo Simulations 22
3.4.1 Models 22
3.4.2 Results and discussion 26
3.4.3 Conclusion 36
4- Non Invasive Prototype 39
4.1 Prototype Description 39
4.2 *In vitro* validation 39
4.2.1 Methods 39
4.2.2 Results and discussion 40
4.3 *In vivo* validation 46
4.3.1 Methods 46
4.3.2 Preliminary results 46
4.4 Conclusions 47
5- Invasive Prototype 49
5.1 Prototype Description 49
5.2 Software Interface 49
6- Final conclusions and Future work 51
6.1 Conclusions 51
6.2 Future work 51
Appendices 53
Appendix I – Phantom model-Monte Carlo simulations results 53
Appendix II – Mesurements depth results of Fredriksson *et al* [19] 62
Appendix III – *In vitro* results of the prototype 63
References 69

Figures list

Figure 1: Skin microcirculation organization (artistic representation adapted from Morales (2005)). 5

Figure 2: Single scattering event, vectors and angles involved. A photon with a propagation vector $\boldsymbol{ki}$ collides with a moving particle with velocity $\boldsymbol{v}$, gaining a new wave vector, $\boldsymbol{ks}$, with different frequency. The difference between $\boldsymbol{ki}$ and $\boldsymbol{ks}$ is denominate as $\boldsymbol{q}$, and it is known as scattering vector and the velocity component in the plane of scattering is denoted $\boldsymbol{v}//$. The angle of scattering is represented as θ, the angle between $\boldsymbol{q}$ and v is denoted as $\boldsymbol{\varphi}$, the angle between $\boldsymbol{v}$ and the plane of scattering is α, and ψ is the angle between $\boldsymbol{v}//$ and $\boldsymbol{ki}$ 7

Figure 3: Effect on the Doppler power spectrum when the velocity (a) and when the RBC tissue fraction (b) varies. 9

Figure 4: LDPM (a) and LDPI (b) flowmeter schematics. 11

Figure 5: MONTECARL 2012 software 14

Figure 6: Directions available for the entrance of the beam where F is the focus of the beam, and θ and $\boldsymbol{\varphi}$ are the spatial tilting angles of the symmetry axis of the beam. 18

Figure 7: Scattering system. The incoming and scattered wave vectors are denoted by k_0 and k_s, respectively. θ is calculated by choosing R and using a cumulative function of the scattering function with values between 0 and 1; $\boldsymbol{\varphi}$= R.2π 19

Figure 8: Simulation phantom model: it consists of three main layers a), b) and c). The upper layer, a), is composed microtubes with skimmed milk as moving fluid; the two deeper layers, b) and c) mimic the aluminum plate. 23

Figure 9: Fibre distance vs. mean depth Doppler for different concentrations of milk on the phantom model @ milk velocity 4.68 mm/s. 27

Figure 10: M1 vs. emitting-receiving fibre distance, on the phantom model @ 25% milk concentration. 29

Figure 11: Running graphics of the simulation process. a) 25 photons injected and b) 13128 photons injected. 30

Figure 12: Perfusion vs. Velocity for: a) 25% ; b) 50% aqueous milk solutions and c) milk; and for: d) 0.14 mm; e) 0.25 mm and f) 1.2 mm emitting-receiving fibre distances. Results were taken using the acrylic phantom. 42

Figure 13: Perfusion vs. Velocity for: a) 25%; b) 50% aqueous milk solutions and c) milk; and for: d) 0.14 mm, e) 0.25 mm and for f) 1.2 mm emiting-receiving fibre distances. Results were taken using the Teflon® phantom, with Perimed. 44

Figure 14: Perfusion vs velocity for: a) 785 nm laser light and milk. b) 635 nm laser light and 0.25 mm source detector fibre distance. 46
Figure 15: Signal collected in the human forearm with the non-invasive prototype with: a) 635; b) 785; c) 830 nm laser diode and d) with the commercial flowmeter. 47
Figure 16: Graphical user interface developed for real time perfusion measurements in rats brains. 50
Figure 17: Perfusion vs. Velocity for: a) 0.14 mm, b) 0.25 mm and c) 1.2 mm emitting-receiving fibre distance. Perfusion vs. Velocity for: d) milk, e) 50% and f) 25% of milk concentration for signals collected using 635 nm laser light source. 63
Figure 18: Perfusion vs. Velocity for: a) 0.14 mm, b) 0.25 mm and c) for 1.2 mm emitting-receiving fibre distance. Perfusion vs. Velocity for: a) milk, b) 50% and c) 25% of milk concentration for signals collected with 785 nm laser light. 65
Figure 19: Perfusion vs. Velocity for: a) 0.14 mm, b) 0.25 mm and c) 1.2 mm emiting-receiving fibre distance. Perfusion vs. Velocity for: a) milk, b) 50% and c) 25% of milk concentration for signals collected with 830 nm laser light sorce. 67

List of tables

Table 1: Teflon and milk optical properties used in the phantom simulation for 635 nm. ……..24

Table 2: Thickness and blood concentration for the three velocity components for each layer in the skin model (adapted from Fredriksson *et al* [17]). ……..24

Table 3: Optical properties for the six skin layers and oxygenated blood (hematocrit=42%) used in skin simulations for 635, 785 and 830 nm, laser beams. ……..25

Table 4: Gray matter, oxygenated and deoxygenated blood optical properties used in the rat brain simulation for 785 nm. ……..26

Table 5: The mean depth of the Doppler events for each photon, the percentage of Doppler shifted detected photons and the mean of Doppler scattering events for each photon for the phantom model, with milk pumped at 1.56 mm/s. ……..28

Table 6: The average path number, the average path depth and the mean path length for photon for the phantom model, with milk pumped at 1.56 mm/s. ……..32

Table 7: The mean depth of the Doppler events for each photon, the percentage of Doppler shifted detected photons and the mean of Doppler scattering events for each photon for the skin model. ……..33

Table 8: Doppler events percentage in each layer. ……34

Table 9: First order moment (M1) of Doppler power spectrum for skin model. ……..35

Table 10: The average path number, the average path depth and the mean path length for photon, using the skin model. ……..36

Table 11: The mean depth of the Doppler events for each photon, the mean of Doppler scattering events for each photon, the percentage of Doppler shifted detected photons and M1 for the rat model. ……36

Table 12: Statistics of linear regression obtained in the acrylic phantom with Perimed. *m* and *b* are the one and zero degree polyminal coefficients, respectively, of the linear fitting. ……42

Table 13: Statistics of linear regression obtained in the Teflon® phantom with Perimed. *m* and *b* are the one and zero degree polynomial coefficients, respectively, of the linear fitting. ……45

Table 14: The percentage of Doppler events detected, the mean of Doppler scattering events and the mean depth of the Doppler events for each photon for the phantom model (fibre distance and velocity pairs), with skimmed milk (100%). ……53

Table 15: The percentage of Doppler events detected, the mean of Doppler scattering events and the mean depth of the Doppler events for each photon for the phantom model (fibre distance and velocity pairs), with aqueous milk solution (50%). ……54

Table 16: The percentage of Doppler events detected, the mean of Doppler scattering events and the mean depth of the Doppler events for each photon for the phantom model (fibre distance and velocity pairs), with aqueous milk solution (25%). ……55

Table 17: First moment of Doppler power spectrum (M1) obtained in the phantom model (fibre distance and velocity pairs), with milk (100%). ……..56

Table 18: First moment of Doppler power spectrum (M1) obtained in the phantom model (fibre distance and velocity pairs), with aqueous milk solution (50%). ……..57

Table 19: First moment of Doppler power spectrum (M1) obtained in the phantom model (fibre distance and velocity pairs), with aqueous milk solution (25%). ……..58

Table 20: The average path number, the average path depth and the mean path length for photon for the phantom model using a aqueous milk solution at 25%. ……59

Table 21: The average path number, the average path depth and the mean path length for photon for the phantom model, using aqueous milk solution at 50%. ……..60

Table 22: The average path number, the average path depth and the mean path length for photon for the phantom model, using a solution of milk. ……61

Table 23: Measurements depth for skin model obtained by Fredriksson *et al.* [19] Table adapted from table 9 from Fredriksson *et al*[19]. ……62

Table 24: Statistics of linear regression obtained in the acrylic phantom with 635 nm laser light source. *m* and *b* are the polynomial coefficients (one and zero degree, respectively) of the linear fitting. ……64

Table 25: Statistics of linear regression obtained in the acrylic phantom with 785 nm laser light source. m and b are the polynomial coefficients (one and zero degree, respectively) of the linear fitting. ……66

Table 26: Statistics of linear regression obtained in the acrylic phantom with 830 nm laser light. *m* and *b* are the polynomial coefficients (one and zero degree, respectively) of the linear fitting. ……68

Abbreviations

LDF	Laser Doppler flowmeter
LDPM	Laser Doppler perfusion monitoring
LDPI	Laser Doppler perfusion imaging
PU	Perfusion units
Perf	Perfusion
RBC	Red blood cells
CMBC	Concentration of moving red blood cells
C_{RBC}	Concentration of red blood cells
MC	Monte Carlo
NA	Numerical aperture
M0	Zero order moment
M1	First order moment

1 - Introduction

1.1 Motivation

Two laser Doppler flowmeter prototypes that are being built at the Electronic Instrumentation Group within the projects PTDC/SAU-BEB/101719/2008 and PTDC/SAU-NEU/101726/2008 co-financed by FEDER give rise to this thesis project. The first one is for non invasive in-depth human skin blood perfusion monitoring, and, the other is for invasive rat brain blood flow evaluation.

Disturbance in the skin blood microcirculation is a frequent complication in a number of common diseases including diabetes, arteriosclerosis and Raynaud's phenomenon.[34] The interest of clinicians dealing with microcirculation is focussed on the blood flow discrimination between superficial (nutritional blood flow) and deeper (thermoregulatory blood flow) layers of the tissue.[33] Among the few diagnostic techniques available for these blood flow measurements, Laser Doppler Flowmetry (LDF) has been the one that have had the greatest developments, in the medical perspective. However, in spite of the important advantage of real-time monitoring, the laser-Doppler technique has limitations that restrict its clinical usefulness.[33] One of the main problems is the difficulty in estimating the measurement depth in the tissue under investigation.[33,34] Therefore, a measurement system able to evaluate depth discrimination of blood perfusion has become of great interest. Some previous studies suggest the use of different optical arrangements of Laser Doppler probes, specially various emitting-receiving fibres distances, and different wavelengths of emitting laser light.[33,34] Based on this knowledge, a new non invasive laser Doppler flowmeter prototype was constructed in order to add skin depth discrimination capabilities to LDF technique.

Invasive LDF probes are also being used for perfusion studies on internal organs. However, the laser Doppler probes for invasive evaluations, available on the market, with 450 μm of external diameter are too large for, for instance, rat brain perfusion measurements, causing considerable damage to the brain tissue.[34] For that

reason, a new prototype with a microprobe with 260 µm diameter is being built for invasive blood flow measurements in rat brain.

1.2 Purpose

The scope of this work is the validation of two new laser Doppler flowmeter prototypes using Monte Carlo simulations: the non-invasive prototype is a multi-wavelength laser Doppler flowmeter with different spaced detection fibres that will add depth discrimination capabilities to LDF skin monitoring; the invasive prototype is a self-mixing based laser Doppler flowmeter for brain perfusion estimation. In order to do so, these two prototypes have been simulated, using Monte Carlo technique. Measurements made with the non-invasive prototype in the phantom and in the skin will be compared with the simulated Monte Carlo results.

1.3 Thesis structure

This thesis is organized in 5 chapters.

In chapter 1 a general introduction is made where the motivation and the purposes of this work are explained.

A detailed description of LDF technique is made in chapter 2: a short historical background; human skin physiology and its microcirculation processes; a theoretical analysis over the LDF technique; and, the main applications, as well as, the main limitations of the technique are pointed out and described.

An explanation of the Monte Carlo method is made in chapter 3. A brief introduction to the method is made, as well as, its usefulness in the context of this thesis. The principles of light absorption and scattering, and the software used for the simulations are also described. The different simulated models, the obtained results and their discussions are presented.

In chapter 4 *in vitro* and *in vivo* validations of the non-invasive prototype are shown. This chapter presents the non-invasive prototype, the complete description of *in vitro* validation, and the obtained results and conclusions.

The invasive prototype is presented in chapter 5 where it is also made a description of the interface used for the real time signals acquisition.

Final conclusions and the future work are presented in chapter 6.

2 - Laser Doppler Flowmetry

2.1 Introduction

Laser Doppler flowmetry (LDF) is a continuous and real-time method for tissue blood flow monitoring, utilizing the Doppler shift of laser light as the information carrier.

2.2 Historical background

The laser, developed in the middle of the last century, soon found its role in medicine, where it has been frequently used both in therapy and diagnosis. The first experimental studies using LDF were performed in the seventies. It was first applied on retinal blood flow (Riva *et al*.[31]) but was soon extended to other tissues (Stern *et al.*[32]). The original method has been improved through the years and several instrumentation setups have been developed. In the early 80's the fibre-optic based laser Doppler perfusion monitoring (LDPM) technique was introduced. This method allows for temporal perfusion measurements in a small sampling volume. For spatial measurements another technique was developed, the Doppler perfusion imaging (LDPI). This technique creates an image of spatial variability of blood perfusion by scanning the surface of the tissue with a laser beam. Nowadays both LPDM and LPDI instruments are commercially available.[1]

Currently LDF instruments are not routinely used in health care, however LDF has proved to be very useful in research. Experimental investigations and clinical trials have been undertaken on many organs in a variety of disciplines. The mostly commonly investigate organs include the kidney, the liver, the brain and the skin. Among the clinical applications, wound healing, skin disease research, pharmacology trials and Raynaud's phenomenon are frequently represented in the literature.[1,8]

2.3 Medical background

2.3.1 Structure of the skin

The skin is the largest organ in the human body functioning as a blood reservoir. It represents an important physical defence against the external

environment and it is responsible for the body temperature regulation, among others functions. In adults, the human skin has an average thickness of 1-2mm, consisting in two different layers: the epidermis and the dermis. The hypodermis is a layer located below dermis, but it does not make part of the skin.[3]

The epidermis is the superficial thin layer with a thickness varying from 50 to 400 μm, and it functions as a protecting cover. It has no blood vessels but contains melanin, a chromophore, which highly contributes to the colour of the skin and to the absorption contribution of this layer. The light absorption by the human melanin pigment is higher around 335 nm and it is almost null for wavelengths longer than 700 nm. Therefore, the epidermis is transparent to near-infrared radiation.[3]

The dermis is the deeper and the thicker layer and its microvasculature consists of two horizontal plexus: the superficial subpapillary plexus and the profound cutaneous plexus. The superficial subpapillary plexus is located at 400-500 μm from the surface and it gives nutritional support to the epidermis by its capillary loops.[2,3] This superficial plexus got its name from the papillary configuration of the region, where epidermis and dermis are connected and blood is delivered to the active epidermal region. The blood flow in the superficial plexus is then referred as nutritional flow. The cutaneous plexus is located at about 1.9 mm from the surface of the skin and it is connected to the superficial plexus by ascending arterioles and descending venules. In some areas of the body, like nose and lips, it can be found interconnections between these two plexus provided by vascular shunts, called arteriovenous anastomoses (AVAs).[2,3] These shunts are responsible for the body temperature regulation by decreasing or increasing the blood flow through the skin. This blood flow is referred as thermoregulatory flow and it prevents the body from large temperature changes.

The region between the subpapillary plexus and cutaneous plexus is called reticular dermis and consists of dense connective tissue of collagen and elastic fibres, providing the skin strength, elasticity and extensibility.[2,3] In this region, the blood vessels are perpendicular to the skin connecting both plexus. Notice that in the superficial subpapillary plexus and in the cutaneous plexus the blood flow parallel to the skin contrary to what happens in reticular dermis.[2,3]

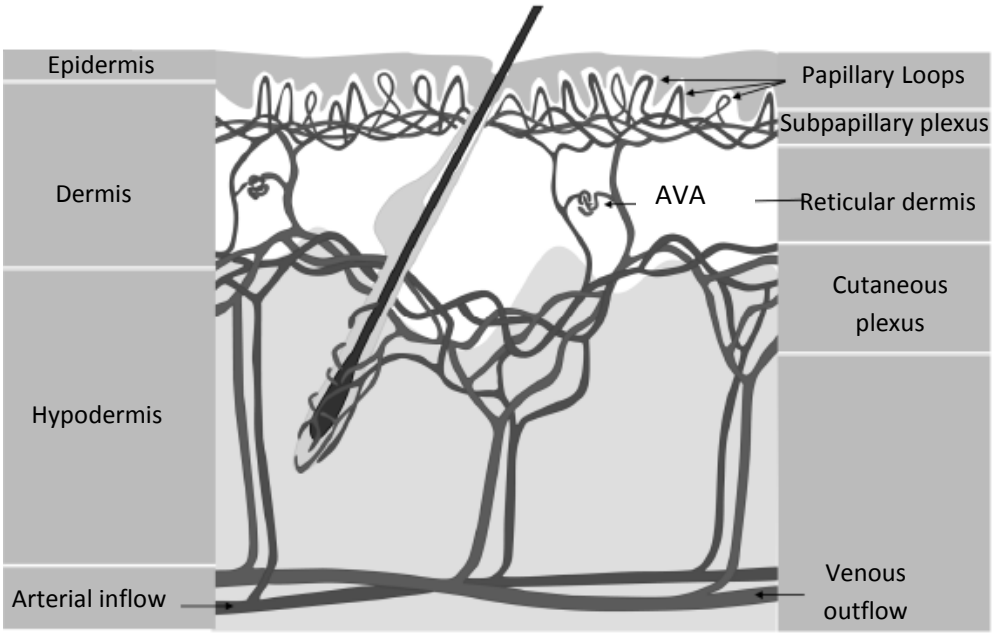

Figure 1: Skin microcirculation organization (artistic representation adapted from Morales (2005)[2]).

2.3.2 Skin microcirculation

All living cells in the body are supported with oxygen and nutrients via the blood. The blood is oxygenized in the lungs and pumped out to the body by the heart. From the heart, the blood is pumped to the aorta which successively branch into smaller arteries, arterioles, till finally branch into capillaries. In the capillaries, gaseous substances and nutrients exchanges with the cells, takes place. After these exchanges, the blood return to the heart through venules, which join larger and larger veins until finally enter into the heart by the venae cavae.[3]

The microcirculation is usually defined as the blood flow through vessels whose diameter is smaller than 100 μm[2,3], including arterioles, venules and capillaries. The microcirculatory flow is controlled by the autonomous nervous system, but variations in concentration of blood dissolved gases, temperature and pressure also affect it. These *stimuli* change the blood flow of the arterioles by vasoconstriction or vasodilatation regulation.

Functional drawbacks in the skin microcirculation may occur due to several diseases, and in some severe cases ulcers and skin necrosis may actually be developed. That is why perfusion of the skin needs to be studied, preferentially with non invasive methods, which have minimum influence on the parameters under study, allowing real time measurements in a clinical environment.[2]

2.4 Theoretical analysis

2.4.1 Light source

The light used in LDF must be monochromatic, i.e., with an extremely narrow frequency band. This way, the Doppler shifted photons will have a detectable frequency broadening when compared with the frequency of the original monochromatic light. The illuminating source should be coherent in time and space, ensuring that the light waves have the same frequency, phase, amplitude and direction. Coherence and monochromacy are properties of laser light, making the laser the proper lighting source for Doppler flowmetry technique.[4]

The wavelengths normally used are 633nm (red) and 780, 810-850nm (near-infrared). These long wavelengths are in therapeutic window,[12] exhibiting a deeper penetration depth, due to the low absorption of melanin, oxygenated and de-oxygenated blood and water.[3,5,12]

2.4.2 Doppler shift and light interaction with the tissue

When a wave interacts with a moving particle its frequency changes. This was first described by Johan Christian Doppler in 1842 and since then it is called as Doppler Effect.

The frequency shift of the scattered light, also known as light Doppler shift, depends on the velocity of the object, the direction of the incoming light and the direction of the scattered light. The angular frequency shift, for a single scattering event, is given by the expression:

$$(2.1)\quad \beta_D = -\boldsymbol{\nu} \times \boldsymbol{q} = -\boldsymbol{\nu} \times (\boldsymbol{k_i} - \boldsymbol{k_s}) = -\frac{4\pi}{\lambda} |\nu| \sin\left(\theta/2\right) \cos(\varphi) \cos(\alpha) \quad (rad/s)$$

where $\boldsymbol{k_i}$ describes the propagation vector (rad/m) of the incoming photon hitting a scattering particle with velocity $\boldsymbol{\nu}$ (m/s) and $\boldsymbol{k_s}$ the propagation vector of the photon after being scattered. The scattering vector, $\boldsymbol{q}$, is the difference between, $\boldsymbol{k_i}$ and $\boldsymbol{k_s}$ ($\boldsymbol{k_i} - \boldsymbol{k_s}$), respectively. Moreover, λ represents the wavelength (m) of the incoming photon in the surrounding medium (eg. tissue), θ is the scattering angle, φ is the angle between $\boldsymbol{q}$ and $\boldsymbol{\nu}$ and finally, α represents the angle between $\boldsymbol{\nu}$ and the scattering plane.[1]

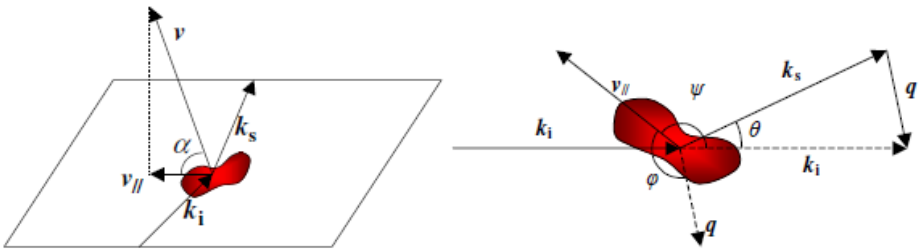

Figure 2: Single scattering event, vectors and angles involved. A photon with a propagation vector $\boldsymbol{k_i}$ collides with a moving particle with velocity $\boldsymbol{v}$, gaining a new wave vector, $\boldsymbol{k_s}$, with different frequency. The difference between $\boldsymbol{k_i}$ and $\boldsymbol{k_s}$ is denominate as $\boldsymbol{q}$, and it is known as scattering vector and the velocity component in the plane of scattering is denoted $\boldsymbol{v}_{//}$. The angle of scattering is represented as θ, the angle between $\boldsymbol{q}$ and **v** is denoted as $\boldsymbol{\varphi}$, the angle between $\boldsymbol{v}$ and the plane of scattering is α, and ψ is the angle between $\boldsymbol{v}_{//}$ and $\boldsymbol{k_i}$.[1]

When analysing the expression (2.1) it is obvious that the frequency shift is linearly dependent to the velocity and it is maximum when the scattering angle θ is equal to ±π (rad), i.e., when the direction of the moving particle and the incident light are equal or opposite.

In biological tissues there are various types of cells and substances, with different optical properties. It is considered to be a turbid media where photons are multiple scattered. However, if the tissue is not moving, the flow of red blood cells (RBCs) can be considered the main cause of perceptible frequency shift.[1,3] In this media the wave vector of the incident light, $\boldsymbol{k_i}$, can be considered random when compared to the direction of the blood flow, since several scattering events can happen before the collision with a RBC.[3,4] On the other hand the propagation vector of the scattered light, $\boldsymbol{k_s}$, depends on the propagation vector $\boldsymbol{k_i}$, as the scattering vector θ is typically very small.[1,3] This results in a smaller frequency shift than if all θ had equal probability. However, each photon can be scattered multiple times by the RBCs, resulting in a total frequency shift larger on average. Since $\boldsymbol{k_i}$ is regarded as random, the direction of blood flow is not obtained by this technique.[4]

Besides this, RBCs are very forward scattering particles, which in general gives θ close to zero radians. Consequently, this results in a scattering vector $\boldsymbol{q}$ often orthogonal to the propagation vector $\boldsymbol{k_i}$, and parallel to **v**, when the RBCs move orthogonal to the incoming vector. As **q** is parallel to **v**, this results in a Doppler shift maximized for small scattering angles when the expected is that larger scattering angles generate larger frequency shift, as explained before.[1,3]

2.4.3 Doppler Power Spectrum

This section is based on the theoretical framework presented by Forrester[35], in 1961 and then revised by Cuummins *et al*.[36] and extended by Larsson[37]. Forrester showed how the individual Doppler shifts are linked to the Doppler power spectrum.[1,3]

The detected non-Doppler shifted light photons, and Doppler shifted photons (that undergone a small frequency shift), will both interfere with each other at the detector site. As laser light is coherent, the interference phenomenon will give rise to a speckle pattern.[1,3,4] Since the light frequencies are slightly different between each other, due to the Doppler shifts, this speckle will "move" and rhythmically change intensity in a way that it seems to "beat".[1,6] If we consider, for simplicity, the laser light as being electric field sources with different frequencies, at the surface of the detector a "beating" speckle will be formed resulting from the superposition of those E-fields. On the detector spot, this will generate a current, *i(t)*, linked to the local mixed E-field fraction, E(t):

$$i(t) = k|E(t)|^2 = kE(t)E(t), \tag{2.2}$$

where k is a specific detector constant.[1]

Fredriksson *et al*.[1] stated that the amplitude variations in the detector current can be analyzed by looking at the power spectral density, referred as the Doppler power spectrum, P(ω),

$$P(\omega) \propto I(\beta) * I(\beta), \tag{2.3}$$

where $*$represents the cross correlation and $I(\beta)$ is the optical Doppler spectrum, ie., the frequency content of the detected Doppler shifted light.

Thus, for the entire detector they arrived to the expression:

$$P(\omega) = n_s \cdot k_{ac}^2 \cdot I(\beta) * I(\beta), \quad \omega > 0. \tag{2.4}$$

Here, n_s denotes the number of speckle areas that fit on the detector and k_{ac} is the AC part of the constant k introduced in the expression (2.2)

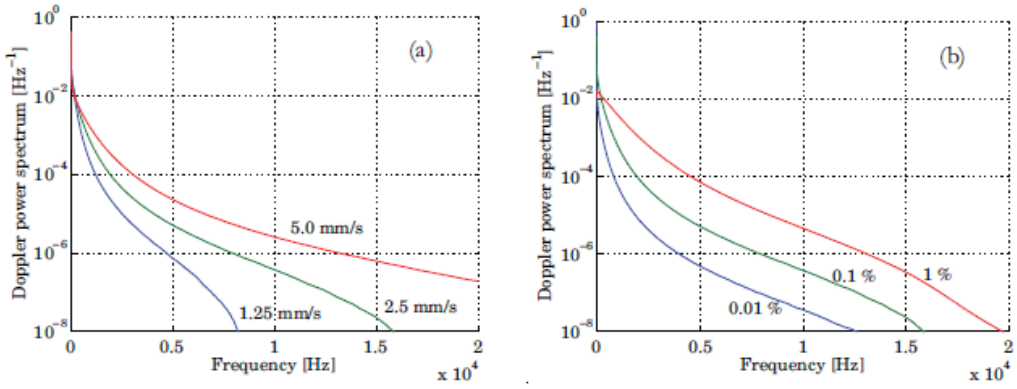

Figure 3: Effect on the Doppler power spectrum when the velocity (a) and when the RBC tissue fraction (b) varies.[3]

2.4.4 Measured variables

The conventional parameters obtained from laser Doppler technique are perfusion, Perf, and concentration of moving red blood cells, CMBC. Perfusion, is defined as the concentration of red blood cells (C_{RBC}) times its average velocity, $\langle v_{RBC} \rangle$:

$$Perf \propto C_{RBC} \langle v_{RBC} \rangle \ , \tag{2.5}$$

and CMBC scales linearly with C_{RBC}:

$$CMBC \propto C_{RBC}. \tag{2.6}$$

These expressions are valid for low concentration of red blood cells (RBC), only. Otherwise the CMBC and Perf scale nonlinearly with C_{RBC} . On the other hand, the relationship between Perf and $\langle v_{RBC} \rangle$ is completely linear, as long as C_{RBC} is maintained constant and the frequency distribution of the photocurrent is within the bandwidth of the system.[1]

Both of these parameters can be estimate from the Doppler power spectrum.[1] The CMBC is proportional to the zero order moment of the P(ω),

$$CMBC \propto \int_0^\infty P(\omega) d\omega \ , \tag{2.7}$$

and Perf is calculated as the first moment of the P(ω),

$$Perf \propto \int_0^\infty \omega P(\omega) d\omega. \tag{2.8}$$

In equations 2.7 and 2.8, P(ω) represents the power spectrum of the AC component of the light, so, P(ω)=0 when ω=0.[1]

2.5 LDPM and LDPI

As stated in the introduction of this chapter there are two different techniques based on laser Doppler: LDPM and LDPI.

2.5.1 LDPM

In a single point monitor flowmeter, optical fibres are typically used to guide the light from the laser source to the tissue and from the tissue to the detector. Normally separate fibres are used but the same fibre can be use to lead and receive the light to and from the tissue (self-mixing method). This is required when a small volume measurement is needed.[2,3]

When more than one fibre is used, the distance between the illuminating and receiving fibre that are in contact with the skin, influences the measuring depth in such a way that the larger the fibre distance, the deeper the light penetrates in the tissue, and so, more photons that travelled through deeper skin layers are detected. Increasing the fibres distances also tends to increase the average path length of the detected photons. However, a big emitting-receiving distance results in a high degree of multiple Doppler shifts leading to severe non linearity in the conventional CMBC and perfusion measurements.[3,8] The most common emitting-receiving fibre distance provided by the two leading manufacturers of LDF instruments (Perimed AB, Jarfalla, Sweden, and Moor Instruments Ltd, Axminster, UK) is 0.25 mm and their devices commonly use a laser source with a wavelength of 780nm.[3]

2.5.2 LDPI

In a conventional imaging flowmeter a laser beam is scanned over the tissue of interest using a moving mirror to form a 2D image of the tissue perfusion. In each scanning position, a detector typically placed at 20-30 cm above the tissue detects the backscattered light via the same mirror. The perfusion value is then calculated and stored in a computer memory as a pixel value. The scanning procedure lasts for a few minutes and when completed, the system generates a colour-coded perfusion image displayed in a monitor.[8]

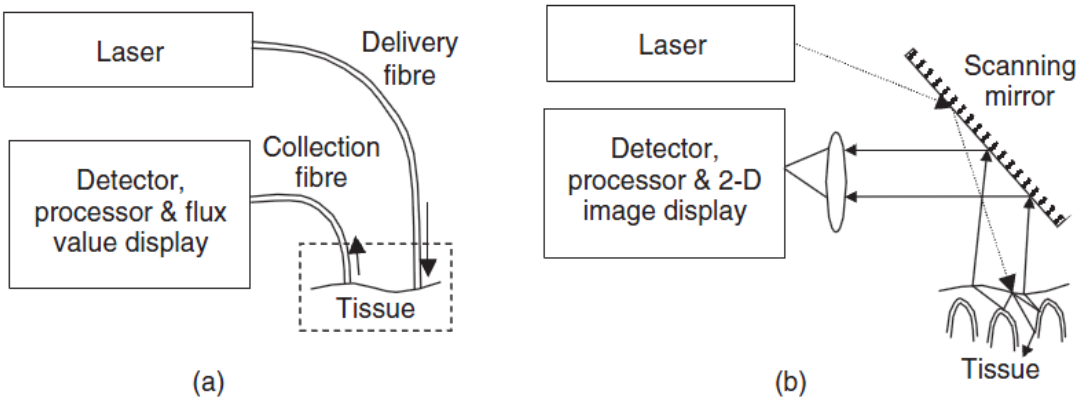

Figure 4: LDPM (a) and LDPI (b) flowmeter schematics.[5]

LDPI has two major advantages over LDPM. Firstly, the blood flow is measured over an area rather than at a single site. Secondly, the laser beam it is not in contact with the skin decreasing the movement artifacts.[5]

2.6 Applications

Functional disturbance in the blood microcirculation is a frequent complication in a number of common diseases. Therefore, a new concept in medicine to use microcirculation, as a window into the physiology and pathology of the circulatory system is growing.[9]

Experimental investigations and clinical trials have been undertaken on many organs and living tissues in a variety of disciplines.[1] The skin is probably the most studied organ and its microcirculation is affected in several ways. The superficial dermal plexus and capillary loops are often affected by diseases such as eczema, psoriasis and acne and little responsive to cardiovascular variations, while the deeper circulation (deep dermal plexus, AVAs) may be more responsive to general cardiovascular adaptations. Furthermore, some complex widespread diseases such as diabetes may act at both levels of microcirculation.[11]

Among other clinical applications the: evaluation of the tissue perfusion in association with Raynaud's phenomenon; the burn wound depth assessment by differentiating between superficial and deep blood flow; the peripheral vascular disease; etc, are frequent.[10,11]

2.7 Technical limitations of LDF

2.7.1 Reproducibility of measurements

In LDPM, a small segment of heterogeneous tissues is sampled, thus, it is impossible to measure on identical locations at different occasions. Moreover, microcirculation is variable in time and it is affected by many factors that cannot be predicted.[2,3]

2.7.2 Absence of measurements units

Currently, LDF cannot express the flux signal in absolute flow units (ml/min) or tissue flow units (e.g., ml/min/100 g tissue), instead an arbitrary unit called perfusion unit (PU) is used. This is due to the impossibility to know the exact tissue volume being probed, the direction of the blood flow and the amount of blood vessels and their length in the measuring volume.[2]

2.7.3 Motion artifacts

As, laser Doppler technique is unable to detect the origin of the light intensity fluctuations, it simply measures it, it is important that the fluctuations caused by Doppler effect actually dominate the signal. Although, movement of the probe relatively to the tissue, local contractions, etc., can contribute for a larger perfusion signal than the perfusion itself. Therefore, motion of the tissue should be avoided during LDF measurements. If this cannot be completely avoided, the signal must provide high time resolution in order to detect the peaks from movements.[2,3]

2.7.4 Biological zero

When recording during arterial occlusion, the flux signal should fall to zero. However, there is always a small flux signal even in the absence of blood flow, which is called biological zero. In other words, the perfusion signal will not be zero even if there is no perfusion in the tissue.[2]

It is believed that the biological zero signal arises from Brownian motion of the cells in the interstitium, vasomotion, and electrical noise.[7] The biological zero is proportional to the tissue temperature between 15 and 37 C, and can be a considerable part of the CMBC signal, especially if LDF is applied on a tissue with low perfusion or if the temperature is greatly increased.[3]

3 - Monte Carlo Method

3.1 Introduction

Monte Carlo (MC) simulations are based on the method of statistical sampling for the solutions of quantitative problems.[13] Among others applications MC method can model the transport of light in the tissue for any arbitrary complex geometry for the medium, light source and detector using random number-based decisions.[3,14]

This method describes and predicts the light transport in a biological media by simulating random paths for a great number of individual photons.[3,14] On its trajectory, each individual photon can be scattered (reflected or refracted) or absorbed. The random path is simulated based on the optical properties of the medium, i.e. the absorption coefficient μ_a, the scattering coefficient μ_s, the scattering phase function, and the refractive index η.[3,13,14] Among the different optical events, the photon will propagate and the optical mean free path in that part of the sample will determine the length of the propagation path.[14]

MC method has been applied in LDF since the early nineties in order to better understand microvascular perfusion and LDF measurements.[14] The simulation of LDF signals is possible because this method allows simulating the interaction of a photon with a moving particle in the sample, causing Doppler shift, which can be registered. Afterwards, from the Doppler shift distribution of all suitable detected photons the frequency power distribution can be derived.[14,15]

This chapter intends to describe, briefly, the software "MONTECARL 2012" (cf. fig 5) developed by Prof. Frits de Mul and used for LDF simulations.[23,24] It will also be described the simulations models used in this work in order to validate the two new laser Doppler prototypes, as well as the obtained results.

Figure 5: MONTECARL 2012 software.[23,24]

3.2 Fundamental optical properties: Absorption and Scattering

In the Monte Carlo method, light is represented as a particle in order to describe light propagation in a turbid media. The particle representation of light offers an intuitive representation of energy transfer, absorption and scattering.

3.2.1 Absorption

Absorption is a process involving the extraction of energy from light by a particle. In each absorption event, the energy of a photon is transferred to a molecule or a single unbounded atom, causing an increase in the molecule or atom internal energy state from one level to another. This energy level shift is called transition and only discrete transitions are allow, as explained by the quantum theory.[19] The absorption process can be of electronic, of vibrational or of rotational nature, considering that the later two can only occur in molecules.[19] The transition energy level is dependent on the structure and composition of the molecule, and therefore, each molecule has a unique absorption spectrum.[19] Biological molecules often have large and complex structure, making the combinations of transitions nearly infinite.[3]

A medium with uniform distribution of absorbing molecules can be quantified by the absorption coefficient μ_a (mm^{-1}),

(3.1) $$\mu_a = \frac{1}{l_a},$$

where l_a is the absorption mean free path and represents the average distance that a photon travels before being absorbed.[19] So, μ_a can be interpreted as the average number of absorption events per mm. The Beer-Lambert's law:

(3.2) $$I = I_o e^{-d\mu_a},$$

describes how light intensity (*I*) decays with the penetration distance (*d*) through an absorbing material, with absorption coefficient, μ_a, where I_o is the intensity of incident light.[3]

3.2.3 Scattering

The scattering of light may be thought of as the redirection of light that takes place when an electromagnetic (EM) wave (i.e. an incident light ray) encounters an obstacle or non-homogeneity. When the homogeneity of the medium is disturbed, a local change in the refractive index occur, causing the light to propagate in other directions different from the forward direction – the scattering occurs.[3,19] The scattering angle is strongly dependent on the size and shape of the objects. Actually, scattering is classified into the following three categories, defined by the size of the scattering object relative to the wavelength:

- Rayleigh limit, where the size of the scatterer is much smaller when compared with the laser light wavelength, applicable to small, dielectric (non-absorving) particles;[19,20]
- Mie regime, commonly used when the size of the scatterer is similar to the laser light wavelength. Although, is applicable to spherical particles at any size-to-wavelength ratio;[19]
- Geometric limit, where the size of the scatterer is much larger when compared with the laser light wavelength. At this limit, reflection and refractive transmission occur.[19] A fraction of light is reflected at the boundary and the remaining light is transmitted through the boundary with a deterministic angle. The relation between the angle of incidence and the angle of refraction for the transmitted light is given by Snell's law:

  (3.3) $$\sin\theta_2 = \frac{n_1}{n_2}\sin\theta_1,$$

where n_1 and n_2 are the refractive index of the object and surrounding medium, and θ_1 and θ_2 are the angles of incidence and refraction, respectively.[19]

In analogy with absorption, a medium containing an uniform distribution of identical scatterers is characterized by the scattering coefficient, μ_s,

(3.4) $$\mu_s = \frac{1}{l_s},$$

where l_s is the scattering mean free path and represents the average distance that a photon travels between consecutive scattering events.[12,19]

Besides the scattering coefficient, also the anisotropy factor *g* and scattering phase function, $p_s(\theta)$, are used to describe a scattering medium. The anisotropy factor, g, represents the mean cosine of the scattering angles θ and describes the level of forward scattering. A value near zero indicates equal amounts of forward and backward scattering. In opposition, a value near one indicates strong forward scattering, i.e., a small change in the propagation direction.[3] The scattering phase function describes the distribution of scattering angles. The most common phase function used in bio-optics is the Henyey-Greenstein (HG) phase function, which has been found to resemble the phase function of many biological tissues.[3,12] Since, HG phase function can be written in a closed analytical form, it can be used as a fast replacement for the Mie-functions that are incapable to calculate the phase function of biological tissues due to their complexity. HG is expressed by the probability function:[3,12]

(3.5) $$p_{HG}(\theta) = \frac{1}{4\pi}\frac{1-g^2}{(1+g^2-2g.\cos\theta)^{3/2}},$$

where *g* is the anisotropy factor.

However, Henyey-Greenstein phase function is inaccurate to model red blood cells scattering. Therefore, the two parametric Gegenbauer Kernel phase function was specially developed to describe the phase function of blood and other biological particles and it is given by:[3]

(3.6) $$p_{gk}(\theta) = \frac{\alpha_{gk} g_{gk} (1-g_{gk}^2)^{2\alpha_{gk}}}{\pi\left(\left(1+g_{gk}\right)^{2\alpha_{gk}}\right) - (1-g_{gk})^{2\alpha_{gk}} (1+g_{gk}^2-2g_{gk}\cos\theta)^{\alpha_{gk}+1}},$$

where $\alpha_{gk}$and g_{gk} are the only parameters that influence the phase function.

In order to describe a scattering medium the reduced scattering coefficient μ'_s can be used. This coefficient combines the scattering coefficient and the anisotropy factor, allowing to describe the medium as an isotropic scattering, i.e., equal scattering events happen in all directions,

(3.7) $$\mu'_s = \mu_s (1 - g)^3.$$

3.3 Software description

3.3.1 Simulation initialization

Before starting the simulations some preparations are firstly needed, namely:[14,15]

- Characterization of the particles (optical properties, concentrations, velocities, etc);
- Calculation of the angle-dependent scattering functions for all types of particles;
- Characterization of the light source, either a pencil beam, a broad divergent beam or an internal source;
- The simulation model, consisting of one or more layers with different objects, with different optical characteristics and velocity profiles. The objects may consist of cylinder, sphere, cone, and rectangular block arrays, or mirrors;
- Characterization of the detection system, consisting of a poly-element detection window, and its numerical aperture;
- Characterization of the calculation mode: *e.g.* reflection, or transmission, or absorption, or a combination of those;
- Extra features, like Laser Doppler Flowmetry.

3.3.2 Light Sources

For the photons injection, various mechanisms are possible. Most general is the pencil beam, entering from the top of the simulation model. The only programming requisite of this beam is to define the point of injection at the sample surface. The photons can then be tilted in two directions, which can be described using the polar and azimuthal angles, θ and φ, respectively (Fig 6).[15]

De Mul software also offers other beam profiles, such as, broad beams, ring shaped beams, isotropic injection and internal point sources.[14,15]

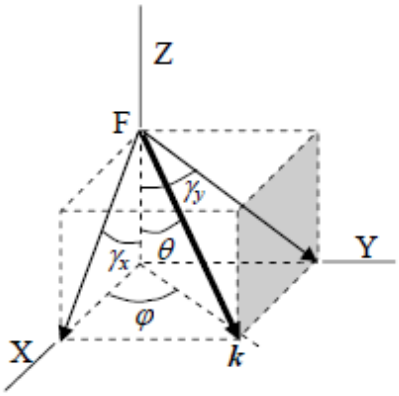

Figure 6: Directions available for the entrance of the beam where F is the focus of the beam, and θ and $\boldsymbol{\varphi}$ are the spatial tilting angles of the symmetry axis of the beam.[15]

3.3.2 Algorithms applied to light transport in tissue

Along the travel of the photons through the sample, they may suffer: scattering or absorption, reflection or refraction at boundaries, and detection. For these, algorithms are needed to implement them. Additionally, the destruction of irrelevant photons (e.g. photons that have travelled extremely far from the detection window) is considered.[14,15]

Propagation

The average translation distance for a photon in a layer or block l with different scattering particles, when there is no absorption in that layer itself, is:

(3.8) $$L_l = \frac{1}{\sum_v (c_{lv}\sigma_{tv})},$$

where c_{lv} and σ_{tv} represent the concentration (particles/mm^{-3}) and the total cross section (μm^2) of particle v in layer, respectively.[15]

From this expression Prof. Frits de Mul,[15] deduced the expression for calculating the actual path length Δ*p*:

(3.9) $$\Delta p = L_l \times \ln(1 - R),$$

where R is a random number (0 ≤ R < 1), used for the probability f_s (0< f_s≤ 1) to arrive at a path length Δ*p:*

(3.10) $$f_s = 1 - \exp(-\Delta p / L_l).$$

However, if a boundary at an interface is met this path might end prematurely. In this case, it can be geometrically calculated a path fraction f_p, using the distance

between the previous event point and the intersection point of the path with the interface, and define the "effective path" Δpeff, by

(3.11) $$\Delta peff = f_p \times \Delta p.$$

Now the probability for absorption by the medium l before the photon has reached the end of path Δpeff (≤ Δp) can be defined as:

(3.12) $$f_a = 1 - \exp(\mu_a \times \Delta peff),$$

where μ_a is the absorption coefficient.[14]

Absorption in the system may have two origins. It can take place between the particles or by the medium. Added with the scattering originates an "average translation length" and an "average absorption length" for the medium.[14]

Scattering

If the photon is not absorbed during, or at the end of a translation step, the photon will be scattered. The probability of scattering in the direction given by the angles θ and φ is described by the scattering function p(θ, φ).[15] This function is normalized in such a way that the total scattering over the whole 4π (sr) solid angle is unity (Fig 7):

(3.13) $$\int_0^{2\pi} d\varphi \int_0^{\pi} d\theta . p(\theta, \varphi). \sin(\theta) = 1.$$[15]

Several models of scattering function are available: Dipole or Rayleigh; Rayleigh-Gans; Mie; isotropic; and peaked-forward. Models of Henyey-Greenstein and Gegenbauer kernel (which is an extension of a Henyey-Greenstein-function) can also be used.[15] These scattering functions are describe in more detail in the standards book of Van de Hulst.[30]

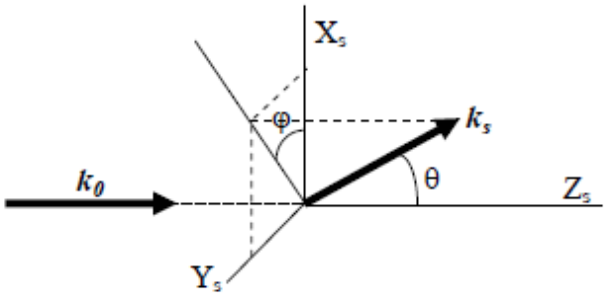

Figure 7: Scattering system.[15] The incoming and scattered wave vectors are denoted by $\mathbf{k_0}$ and $\mathbf{k_s}$, respectively. θ is calculated by choosing R and using a cumulative function of the scattering function with values between 0 and 1; $\boldsymbol{\varphi}$= R.2π.

When polarization effects have to be taken into account, the choice of the angles θ and φ is coupled to the polarization state of the photon.[15]

Boundaries

Since the software allows to choose simulation models with different geometries (e.g. tubes and mirrors) there will be boundaries with flat and/or curved surfaces.

For flat surfaces, parallel to the layer surface, the calculation of reflection or refraction angles is according to Snell's Law. The fraction of reflected light is given by the Fresnel relations.[15]

For curved surfaces, or flat surfaces not parallel to the surface, a new coordinate frame is firstly constructed. In MONTECARL software[23,24] the boundary expressions are derived for following curved surfaces:

- Cylinders;
- Arrays of cylinders (linear or two-dimensions);
- Spheres, and two-dimensions arrays of spheres;
- Rectangular blocks;
- Mirrors.

Absorption

The software used in this work follows the algorithm of "sudden death" to handle non zero-absorption. This method considers that the photon is completely absorbed at once, and thus is removed from the calculation process. Although this method is more time consuming, when comparing with others methods, it allows to study the position where the photon was absorbed.[14,15]

Normally the position of the photon, together with its directional angles, is stored after reflection or transmission.

3.3.3 Detection

The software differentiates between external or internal detection.[15]

Normally the detection of emerging photons takes place at the surface of the sample (either at the top or at the bottom). These external detection options are denoted as "reflection" or "transmission", respectively.[15]

The detection is internal when the photons are supposed to end their path at a certain position inside the sample, e.g. upon an absorption event.[15]

Both options are limited by Numerical Aperture, NA, with $NA = \sin\theta_D$, where θ_D is the half opening angle of the detection cone. NA ranges from 0 (pure pencil beam) to 1 (all incoming angles accepted) and its value must be set in the software.[15]

After a detection event the software stores the detection position of the photon (x,y,z-coordinates) and the direction angles (θ and φ) with respect to the laboratory coordinate frame. It also stores the number of scattering events and the percentage of Doppler scattering events. Furthermore it stores the resulting Doppler frequency and the path length.[15] With external detection the software does not store the z-coordinate of detection, contrary to what was mentioned: it only stores the average depth of all scattering events along the path or, at will, the maximum depth along the path.[15]

In the case of external detection (reflection or transmission) the photon is assumed to be detected if:

- It passes the detection plane in the proper direction. This implies that the photon has crossed the final interface between the sample and the medium where the detector is.[15]
- It passes that plane within the borders of the "detection window". This window can be chosen rectangular, circular or ring-shaped.[15]

Moreover, the software allows choosing the maximum number of photons detected.

3.3.4 Specially Feature: Laser Doppler Flowmetry

LDF was the oldest feature incorporated in the MONTCARL software[23,24], build in at the beginning of its development. Each individual Doppler shift is calculated using the wave representation of light (see chapter 2) and Doppler shift of each photon. It is, then, stored as an extra attribute of the photon, in the Monte Carlo simulation. The construction of the Doppler power spectrum is based in the frequency distribution of all photons.[15]

The two power spectra moments describe in chapter 2, the zero order moment (M0) and the first order moment (M1) may be calculated. It is also possible to calculate the reduced moment $M1' = \frac{M_1}{M0}$, which is proportional to the average velocity.[14]

For the implementation of the velocity profiles of the scattering particles, the following options are available:

- Velocity directions along X, Y or Z-axis, or along the block axis, in case of oblique blocks;
- Velocity direction randomised for each scattering event with all particles at the same velocity;
- Uniform, or parabolic (in tubes and rectangular objects only), or they can have a Gaussian distribution. [15]

3.4 Monte Carlo Simulations

3.4.1 Models

Phantom Model

The phantom model was built with the purpose to evaluate, *in vitro*, the non invasive flowmeter prototype response to moving fluid at different depths (as it can be found in skin).[22] The phantom consists of a Teflon® microtube rolled around an aluminium metal piece producing a total of six layers. The inner and outer diameters of the microtube are 0.3 and 0.76 mm, respectively. Commercial skimmed milk has been chosen as a moving fluid, because it has various components that act as scatterers, namely carbohydrates, fat, and protein. Moreover, it does not sediment like microspheres, and it has similar behaviour as intralipid solutions.[25] Finally, milk is easier for handling than blood, and it is cheaper. However, as milk is unstable, the same milk solution was used for one day, only. Milk is pumped in the microtubes with a motorized syringe with different velocities: 1.56, 3.12, 4.68, 6.25, 7.78, and 9.35 mm/s. Different milk solutions were used: milk, and aqueous solutions of 50% and 25% of milk.

The first model consists of three main layers (cf. Fig. 8). The first layer is composed of a set of cylindrical objects equivalent to the six microtube layers and it has a total depth of 5 mm. The two deeper layers mimic the aluminium plate and have a thickness of 0.1 mm each one. One acts as a scatterer with isotropic semi-spherical

backscattering and the other is a totally reflecting layer. The laser light was considered as a pencil beam shape and it was positioned at the top of the most superficial outer tube. It was used a ring-shaped detecting window and the NA of the optical fibres is 0.37. A parabolic profile was used for the milk flow simulations, where the maximum cylinder axis velocity is twice the mean velocity.

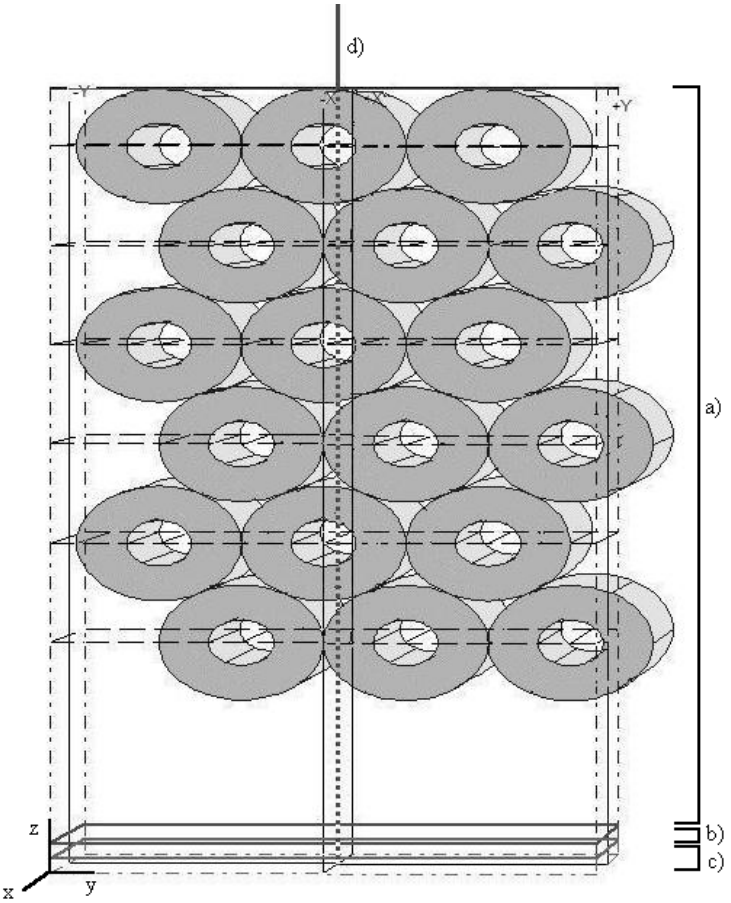

Figure 8: Simulation phantom model: it consists of three main layers a), b) and c). The upper layer, a), is composed microtubes with skimmed milk as moving fluid; the two deeper layers, b) and c) mimic the aluminum plate.

The simulations were made only for 635 nm laser light wavelength, due to the absence of information concerning milk and Teflon optical properties for 785 and 830 nm laser light. The milk optical properties used were published by Waterworth *et al*.[25], where the refractive index for milk is 1.346, μ_a and μ_s are 0.00052 and 52 mm^{-1}, respectively. The Teflon optical properties used were published by Li *et al*.[26], where the refractive index is 1.367, absorption and scattering coefficients are 0.001 and 167 mm^{-1}, respectively. The Henyey-Greenstein phase function was used with g=0.90 for both components.[25,26]

Table 1: Teflon and milk optical properties used in the phantom simulation for 635 nm.

	Refractive index	μ_a (mm^{-1})	μ_s (mm^{-1})	g
Milk	1.346	0.00052	52	0.9
Teflon	1.367	0.001	167	0.9

Simulations were made for four different detection distances (0, 0.14, 0.25, 1.2 mm) and for six different velocities for milk speed. In order to evaluate the effect of the milk concentration, three different milk concentrations (100%, 50% and 25%, in distillate water) were simulated. This gives a total of 54 simulations, with 5,000,000 photons detected in each simulation.

Skin Model

The skin simulations were made for three wavelengths (635, 785 and 830 nm) and for the same three different emitting-receiving fibre separations (0, 0.14. 0.25 and 1.2 mm).

The skin model used was inspired in the model presented by Fredriksson.[17,18] It consists of 6 layers with individual optical properties, variable thicknesses, *t*, and different blood concentration, C_{blood}, at three different flow velocities (see table 1), mimicking the skin structure. Each velocity component has a parabolic distribution with centre velocity at 0.3, 3.0 and 30 mm/s, with random direction. The low velocity component is assumed to primarily represent the capillary flow, therefore, the papillary dermis layer, which only contains capillaries, has just this velocity component.[2,17] The middle velocity component is assumed to be the one of the flow in venules, small veins and arterioles, finally the higher component is assumed to mainly represent the large arterioles, veins and arteries. Due to the elevated number of large vessels in the inferior blood net[2], the high velocity component is higher in this layer.

Table 2: Thickness and blood concentration for the three velocity components for each layer in the skin model (adapted from Fredriksson *et al* [17]).

Layer	*t* (mm)	C_{blood} [%]		
		0.3 mm/s	3.0 mm/s	30 mm/s
Epidermis	0.075	0	0	0
Papillary dermis	0.15	0.2	0	0
Superior blood net	0.15	0.6	0.05	0.001
Reticular dermis	0.80	0.1	0.01	0.0006
Inferior blood net	0.40	0.25	0.035	0.006
Subcutis	10	0.1	0.01	0.001

Oxygenated blood with hematocrit equal to 42% was considered [17] (normal hematocrit values: 36-44% for females and 39-50% for males). The skin and blood optical properties, i.e, μ_a, $\mu_{s'}$ and g, are summarized in table 3 and were based on Fredriksson *et al*.[18] for the wavelengths 635 and 785 nm, whereas for 830 nm they have been based on the results presented by Simpson *et al.*[27] and Prahl[28]. Concerning the scattering functions, the blood was modelled with the Gegenbauer kernel scattering phase function, with α=1 for all wavelengths and g=0.95 mm^{-1} for 635 nm and g=0.948 mm^{-1} for 785 and 830 nm.[18] For static tissue the Henyey-Greenstein phase function was used, with g=0.85 mm^{-1}.[18] The refractive index was set, for all skin layers as well as for blood to 1.4, 1.58 for the probe and 1 for the surrounding air.[18]

The laser light was simulated as an external pencil beam, with a perpendicular entrance in the tissue, and the path tracking was recorded with $1/\mu_s'$ resolution. The numerical aperture (NA) of the fibres is 0.37, and it was chosen a ring-shaped detecting window. A total of 3 times 4 simulations have been made. Ten million photons were detected in each one.

Table 3: Optical properties for the six skin layers and oxygenated blood (hematocrit=42%) used in skin simulations for 635, 785 and 830 nm, laser beams.

Layers	μ_a (mm^{-1})			$\mu_{s'}$ (mm^{-1})			g		
	Wavelength (nm)			Wavelength (nm)			Wavelength (nm)		
	635	785	830	635	785	830	635	785	830
Epidermis	0.15	0.1	0.0122	4.8	3.5	1.81	0.85	0.85	0.9
Papillary dermis	0.15	0.1	0.0122	3	2	1.81	0.85	0.85	0.9
Superior blood net	0.15	0.1	0.0122	3	2	1.81	0.85	0.85	0.9
Reticular dermis	0.15	0.1	0.0122	3	2	1.81	0.85	0.85	0.9
Inferior blood net	0.15	0.1	0.0122	3	2	1.81	0.85	0.85	0.9
Subcutis	0.15	0.1	0.00856	2.4	2	1.12	0.85	0.85	0.9
Blood	0.34	0.5	0.52	2.13	2	2	0.991	0.991	0.991

Rat brain model

The rat hippocampus consists of several substances such as grey matter, white matter and blood vessels, among others. The blood percentage is nearly 4.5% and the white matter is up to 4% of the blood volume. As the percentage of white matter is very low we considered that the hippocampus has 95.5% of grey matter and 4.5% of blood (3.6% of oxygenated blood and 0.9% of deoxygenated blood).[18,29]

The rat brain model consists of 3 scatterers representing the oxygenated and deoxygenated blood, and the grey matter. The optical properties for 785 nm are summarized in table 4 and were based on Fredriksson *et al.*[18]. Concerning the scattering functions, the blood (oxygenated and deoxygenated) was modelled with the Gegenbauer kernel scattering phase function, with α=1 and g=0.948 mm^{-1}. For gray matter the Henyey-Greenstein phase function was used with g=0.85 mm^{-1}.[18] The refractive index was set to 1.4 to all components and the laser light was simulated as a pencil beam with a perpendicular entrance in the tissue and the path tracking was recorded with $1/\mu_s'$ resolution. The numerical aperture (NA) of the optical fibres is 0.11.

The simulations were made only for 785 nm laser light wavelength due to the absence of information concerning optical properties of gray matter, oxygenated and deoxygenated blood for the 1300 nm laser light beam.

Table 4: Gray matter, oxygenated and deoxygenated blood optical properties used in the rat brain simulation for 785 nm.

	μ_a (mm^{-1})	$\mu_{s'}$ (mm^{-1})	g
Grey matter	0.02	0.78	0.9
Oxygenated blood	0.5	2	0.991
Deoxygenated blood	0.64	2	0.991

3.4.2 Results and discussion

Phantom model

The phantom model results, namely the mean depth of the Doppler events per photon, the percentage of Doppler shifted photons detected and the mean of Doppler scattering events per photon are given in table 5 for 1.56 mm/s milk velocity. The complete results of these simulations can be seen on appendix I.

The emitting-receiving optical fibre separation influences the measurements, in such a way, that for larger separations between the fibres, a larger sampled volume is probed. Therefore, increasing the fibre distance, photons travel through deeper objects leading to an increase in the mean depth of Doppler shifted photons (cf. table 5 ahead). Previous studies (Fredriksson *et al.* 2008[17], Fredriksson *et al.* 2009[18]) based on light propagation in living tissues using Monte Carlo computational simulations are in agreement with these results. The same results were obtained for all velocities,

which is explained by the fact that photons path-length are independent of the velocity of the moving fluid. The milk concentration also influences the mean depth, which decreases with the increase of milk concentration (cf. Figure 9). This is due to the higher degree of multiple Doppler shifts registered for higher milk concentrations (see table 5).

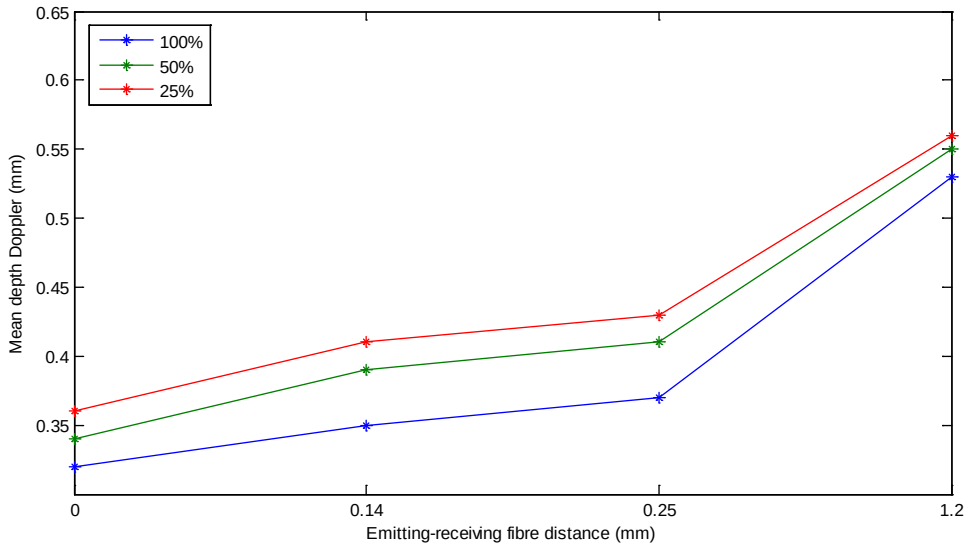

Figure 9: Fibre distance vs. mean depth Doppler for different concentrations of milk on the phantom model @ milk velocity 4.68 mm/s.

The percentage of Doppler shifted photons detected increases with the emitting-receiving separation for each velocity. This is expected, because when the fibre distance increase, the measured sample volume increases, and a larger amount of Doppler shift is detected. Similar results were obtained for all velocities. This means that the amount of light Doppler shifted detected is not influenced by the velocity of the moving fluid, since the concentration is maintained constant. If the concentration of milk increases the percentage of Doppler shifts detected also increases (cf. table 5, ahead). The more concentrated is the milk, the more scatterers are present, and consequently, more scattering events occur.

Likewise, the mean Doppler scattering events per photon also increases with the fibre distance for each velocity. This is not surprising, as we are considering a homogeneous model (for the scatterers velocity and concentration). Therefore, an increase in the sampled volume, will naturally lead to more Doppler scattering events. In what concerns the milk concentration, was already referred that an increase in milk

concentration leads to a higher degree of multiple Doppler scattering, because the higher the concentration, the higher the scatterers presented.

All the mentioned parameters (mean Doppler depth, percentage of Doppler shifted detected photons and mean Doppler scattering) increase with the fibre distance, but the increase is higher for the fibre distance 0.25 to 1.2 than for 0.14 to 0.25 mm (see table 5). This can be justified if we notice that 0.25 is approximately the double of 0.14 while 1.2 is approximately fivefold 0.25, therefore the sample volume measure with a emitting-receiving separation of 1.2 is larger when compare to 0.25, leading to a more significant increase.

Table 5: The mean depth of the Doppler events for each photon, the percentage of Doppler shifted detected photons and the mean of Doppler scattering events for each photon for the phantom model, with milk pumped at 1.56 mm/s.

Milk concentration	Fibre distance (mm)	Mean depth Doppler (mm)	Detected Doppler (%)	Mean scattering Doppler
25%	0	0.36	4.77	3.48
	0.14	0.41	26.00	4.29
	0.25	0.43	41.23	4.37
	1.2	0.56	82.00	6.47
50%	0	0.34	6.73	5.85
	0.14	0.39	32.35	7.30
	0.25	0.4	47.76	7.78
	1.2	0.55	86.00	12.65
100%	0	0.32	10.27	10.08
	0.14	0.35	41.26	12.66
	0.25	0.37	56.45	14.27
	1.2	0.53	87.47	26.63

The first order moment of the Doppler power spectrum, M1, was also evaluated. Figure 10 shows the effect on M1 when the fibre distance increases, for each velocity and, for a concentration of milk of 25%. It can be seen that higher values of M1 have origin from larger fibre separation, whereas the lowers values of M1 are obtained for 0 mm fibre separation. Another observation is that, in general, M1 increases with the velocity and with the milk concentration. This is not surprising because M1 is proportional to perfusion (Perf), which in turn is proportional to the scatterers concentration times their average velocity. However, in some specific cases M1 does not increase with the velocity, especially for the two highest velocities and for 1.2 mm fibre distance. This might be due to because the phantom model that saturates in such extreme situations.

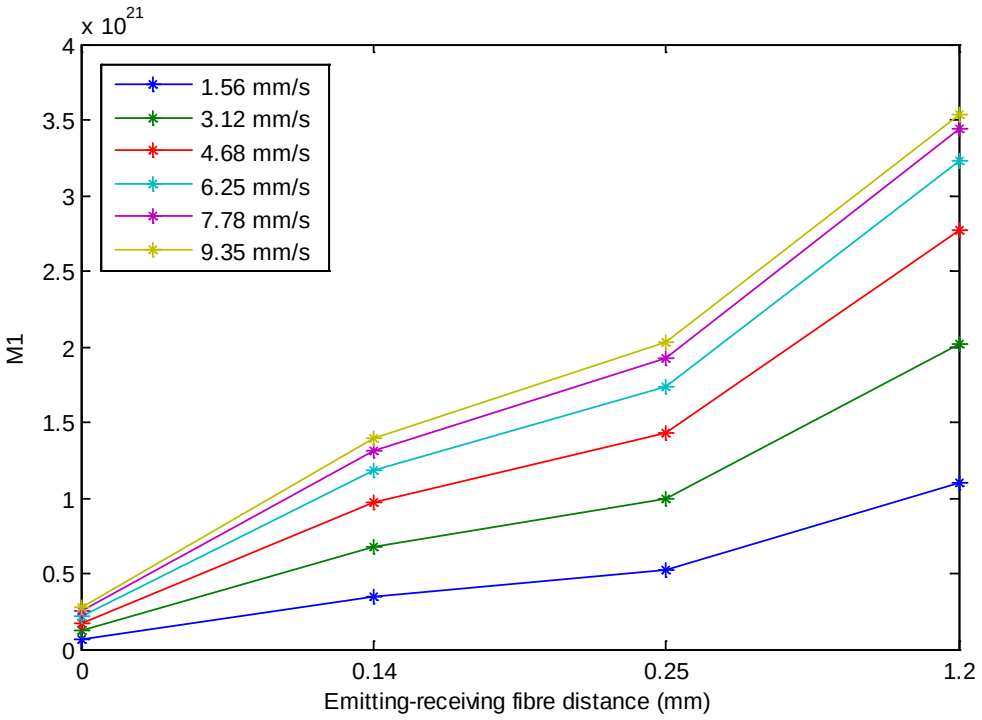

Figure 10: M1 vs. emitting-receiving fibre distance, on the phantom model @ 25% milk concentration.

In order to better understanding the path travelled by the photons, a path tracking study was done. The path tracking can be 'followed' in MC software during the simulations. In Fig. 11 it can be seen the path tracking for 25 [Fig. 11 a)] and 13128 [Fig. 11 b)] photons injected. The photon are injected in (0,0,0) coordinates.

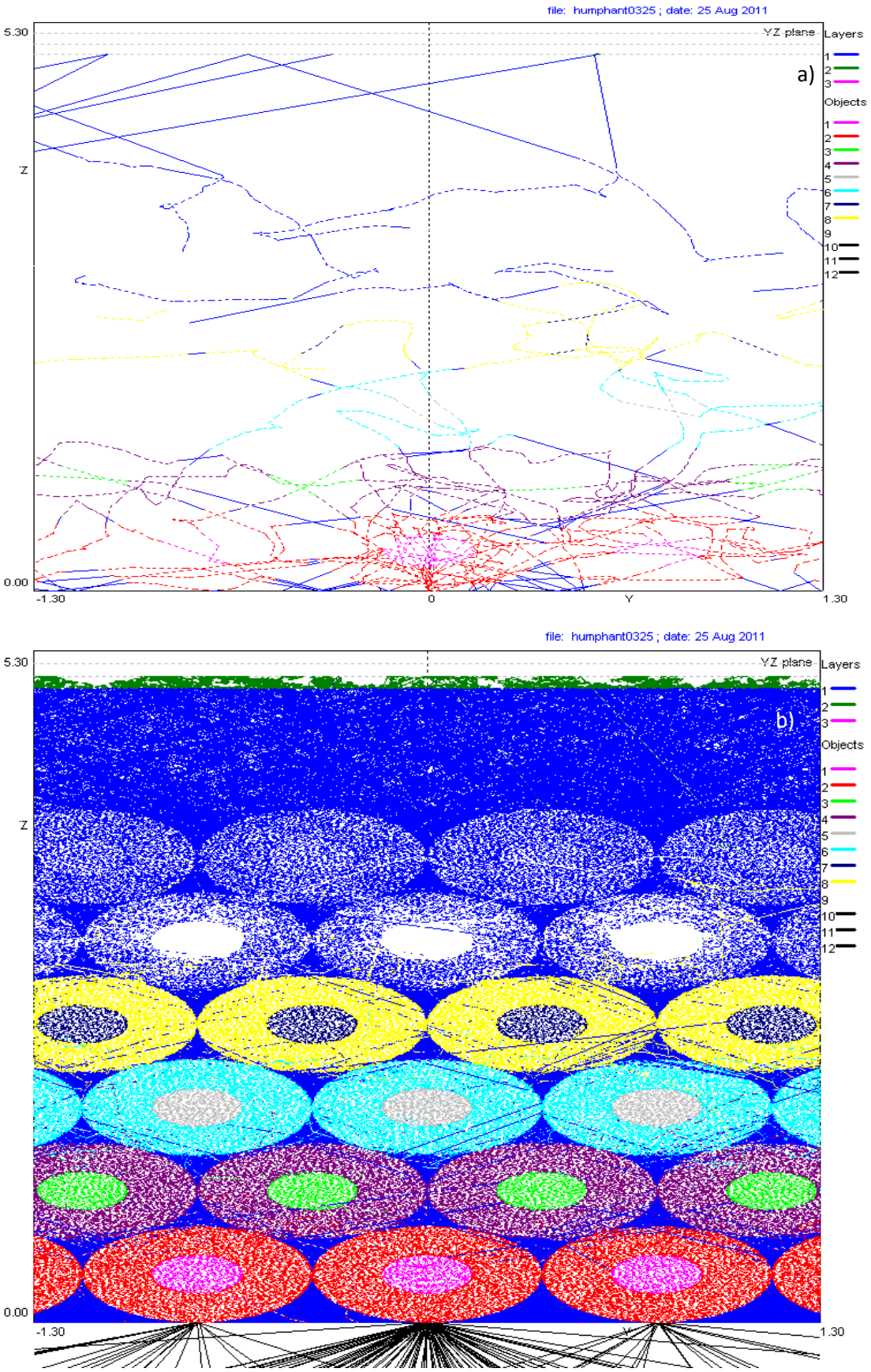

Figure 11: Path tracking registered during the simulations. a) 25 and b) 13128 photons injected.

The average number of paths travelled by each photon and the respective average depth were estimated. Furthermore, the average path length for each photon was also evaluated. The results for 1.56 mm/s are presented in table 6, but all results are presented in appendix I, tables 20, 21, 22.

The average number of paths for each photon increases with emitting-receiving fibre distance (cf. table 6). This is expected because as mentioned, a greater fibre distance allows sampling a greater volume and therefore, a bigger number of paths are registered. Similar results were obtained for different velocities proving that the scattering events are independent of the scatterers velocity, although, for different milk concentrations, there is not a clear tendency for the variation of the number of paths with the milk concentration.

The average path depth for each photon is higher for zero emitting-receiving fibre distances, lowers to 1.2 mm fibre distance, and it is lowest for 0.14 and 0.25 mm fibre distance (which have similar depths) (cf. table 6). The results are similar for different velocities, because this parameter does not interfere with the number of paths. For different milk concentrations there is not a clear tendency for the variation of the number of paths.

Finally, it was evaluated the average path length. This parameter, is higher for zero emitting-receiving fibre distance, lowers to 1.2 mm fibre distance, and it is lowest for 0.14 and 0.25 mm fibre distance (cf. Table 6). The results obtained are similar for all the velocities. A clear tendency for the variation of the number of paths with the milk concentration cannot be observed.

Table 6: Mean path number, mean path depth and mean path length for photons for the phantom model, with milk pumped at 1.56 mm/s.

Milk concentration	Fibre distance (mm)	<Path number>	<path depth> (mm)	<path length> (mm)
25%	0	3.31	1.45	10.66
	0.14	7.00	0.23	2.53
	0.25	9.66	0.23	2.55
	1.2	25.67	0.47	5.95
50%	0	3.37	1.41	10.74
	0.14	7.06	0.24	2.58
	0.25	9.51	0.22	2.45
	1.2	25.91	0.47	6.07
100%	0	3.49	1.41	10.43
	0.14	7.04	0.22	2.53
	0.25	9.53	0.21	2.43
	1.2	27.67	0.45	6.24

Skin Model

The mean depth Doppler scattering events per photon, the percentage of Doppler shifted detected photons and the mean of Doppler scattering events per photon obtained in Monte Carlo simulations, for the skin model, are presented in table 7.

The mean depth for the Doppler events increases with fibre distance, as for the phantom model, because a larger emitting-receiving separation allows sampling a larger volume. It can be noticed that the mean depth of the Doppler shifted photons never reaches the reticular dermis or the layers below this one, since reticular dermis lies at a depth of 1.175 mm (cf. table 2) and the mean depth predicted for the Doppler events is always lower than this value (cf. table 7). Moreover, the measurement depth also increases with the wavelength magnitude. This is due to both skin absorption and scattering coefficients decrease with the wavelength, allowing the photons to travel a longer path. Similar results were obtained by Fredriksson *et al.*[18] (see appendix II), with a measurement depth slightly smaller, but with the same order of magnitude.

The percentage of Doppler shifted detected photons increases with the emitting-receiving fibre distances. As discussed, this is due to the increase of the sampled volume that a higher fibre distance allows to probe. The percentage of Doppler detected photons also increases with the wavelength, except for the 1.2 mm emitting-receiving fibre distance. This may be related with the distribution of the

Doppler events percentage in each layer (cf. table 8). It can be seen that the reticular dermis is the 2nd layer with more detected Doppler photons for 1.2 mm fibre distance (for 785 and 830 nm laser light), whereas for the other fibre distances the 2nd layer with more detected Doppler photons is the papillary dermis. This proves that the photons detected at 1.2 mm from the emitting fibre cross a higher volume of blood. Besides, the Doppler events percentage in the inferior blood net (for 1.2 mm fibre distance) decreases going from 635 to 785 nm laser light and increases going from 785 to 830 nm laser light. This layer has the second higher blood concentration when compared with the other layers. Together, with the higher volume of blood crossed and the increasing of the blood absorption coefficient with the wavelength may cause this nonlinearity.

Similar to what happens with the percentage of Doppler shifted detected events, the mean Doppler scattering per photon also increases with the emitting-receiving fibre distance. This happens, because increasing the fibre distance increases the sampled volume, and, therefore, more scattering events are registered. On the contrary, the mean Doppler scattering event does not follow a general trend when increasing the wavelength of the incident light (c.f table 7) but it is always smaller than 1.5, which means that there are few photons that suffer multiple Doppler shifts.

Similar to what occurs in the phantom model with the analysed parameters, a small increase is observed when we compare 0.14 to 0.25 mm fibre distances and a larger increase is observed when we compare 0.25 to 1.2 mm fibre distance. This is due to the size differences between the emitting-receiving fibre distances used.

Table 7: The mean depth of the Doppler events for each photon, the percentage of Doppler shifted detected photons and the mean of Doppler scattering events for each photon for the skin model.

Wavelength (nm)	Fibre distance (mm)	Mean depth (mm)	Detected (%)	Mean scattering Doppler
635	0	0.24	1.94	1.19
	0.14	0.27	9.62	1.23
	0.25	0.28	15.45	1.26
	1.2	0.37	47.7	1.49
785	0	0.25	1.97	1.16
	0.14	0.29	10.71	1.22
	0.25	0.3	16.29	1.23
	1.2	0.38	41.89	1.41
830	0	0.27	3.54	1.15
	0.14	0.31	14.54	1.23
	0.25	0.33	20.39	1.25
	1.2	0.41	43.45	1.46

Table 8: Doppler events percentage in each layer.

Wavelength (nm)	Fibre distance (mm)	Skin layers					
		Epidermis	Papillary dermis	Superior blood net	Reticular dermis	Inferior blood net	Subcutis
635	0	0	41.07	51.19	7.24	0.50	0
	0.14	0	35.10	53.06	10.31	1.37	0.17
	0.25	0	31.98	55.23	11.1	1.49	0.21
	1.2	0	19.43	56.21	19.51	4.08	0.77
785	0	0	41.73	48.84	8.93	0.51	0
	0.14	0	30.85	54.86	12.97	1.33	0
	0.25	0	27.69	56.42	14.38	1.51	0
	1.2	0	18.81	55.44	22.24	3.51	0
830	0	0	38.76	49.36	10.35	1.54	0
	0.14	0	26.66	55.91	15.09	2.33	0
	0.25	0	23.09	57.05	17.27	2.59	0
	1.2	0	16.57	53.06	25.15	5.21	0

Simulation results also demonstrate that M1 increases with the emitting-receiving fibre distance. Since M1 is proportional to the concentration of moving RBCs times its average velocity, and both parameters increase with the fibre distance, it is obvious that M1 will increase with the fibre distance (cf. table 9).

Table 8 also shows how M1 changes with the wavelength for the different emitting-receiving fibre distance. It can be noticed that M1 decrease from 635 to 785 nm and then increases from 785 to 830 nm. This can be explained if we look at the Doppler photons percentage that exceeds the reticular dermis. This percentage is higher for 830 nm and lower to 635 nm. It is the lowest for 785 nm laser light, with the exception of the 0 mm fibre distance. (cf. table 8). As the inferior blood net has the highest concentration of the high velocity component of RBCs (30 mm/s), resulting in higher Doppler shifts for 635 nm than, for 785 nm photons. Therefore, M1 will be higher for 635 nm than for 785 nm, laser light.

Table 9: First order moment (M1) of Doppler power spectrum for skin model.

Wavelength (nm)	Fibre distance (mm)	M1 (Hz)
635	0	3.57E+18
	0.14	2.51E+19
	0.25	3.71E+19
	1.2	1.63E+20
785	0	3.45E+18
	0.14	2.13E+19
	0.25	3.23E+19
	1.2	1.05E+20
830	0	5.30E+18
	0.14	2.66E+19
	0.25	3.93E+19
	1.2	1.06E+20

Table 10 shows the results of the path tracking study for the skin model. It can be observed that the average path number travelled by each photon increases with emitting-receiving fibre distance. This occurs, because increasing the fibre distance a greater tissue volume is probed, and so, more scattering events occur. On the contrary, the mean path number does not follow a general trend when increasing the wavelength of the incident light.

Mean path depth results are also presented on table 10. It is clear that the mean path depth increases with emitting-receiving fibre distance, as well as, with the wavelength of incoming laser source light. The path depth increases with the fibre distance because the sample volume probed is greater. On the other hand, the path depth increases with the laser light wavelength due to both, skin absorption and scattering coefficients decrease with the wavelength, allowing the photons to travel a longer path. This is in agreement with the mean depth of Doppler events results showed in table 7.

Finally, it was evaluated the average path length. Similar to what happens to the mean path depth and path number, this parameter also increases with the fibre distance due to an increase of the sampled volume probed, allowed by a greater fibre distance. Concerning the wavelength of the incoming light, the average path length increases with the wavelength, excluding for the 1.2 mm emitting-receiving fibre distance. This may be related with the distribution of the Doppler events percentage

in each layer (cf. table 8) as discussed in page 32 and 33 when the percentage of Doppler shifted detected photons was analyzed.

Table 10: Mean path number, mean path depth and mean path length for photons, using the skin model.

Wavelength (nm)	Fibre distance (mm)	<Path number>	<path depth> (mm)	<path length> (mm)
635	0	3.16	0.02	0.23
	0.14	6.1959	0.0775	0.78
	0.25	7.99	0.11	1.16
	1.2	19.77	0.27	4.11
785	0	3.08	0.02	0.23
	0.14	5.98	0.09	0.86
	0.25	7.46	0.12	1.26
	1.2	14.71	0.26	3.65
830	0	3.77	0.04	0.34
	0.14	6.93	0.12	1.12
	0.25	8.34	0.16	1.57
	1.2	14.86	0.28	4.01

Rat model

Only one simulation was done for this model, and the results are summarized in table 11. It can be seen that the Doppler shifted photons travel a mean depth of 0.15 mm. This value is in accordance with Fredriksson *et al*.[18] which obtained 0.16 mm of measurement depth. Each photon suffers, in average, 2.23 scattering events. In a total of 5,000,000 detected photons 11.9% had suffered Doppler shifts, and M1 was predicted to be 3.51E+17. These results will help in the rat brain probe positioning as it will be 0.15 mm above the mean measurement depth.

Table 11: The mean depth of the Doppler events for each photon, the mean of Doppler scattering events for each photon, the percentage of Doppler shifted detected photons and M1 for the rat model.

Mean depth Doppler (mm)	Mean Doppler scattering	Detected Doppler (%)	M1
0.15	2.23	11.9	3.51E+17

3.4.3 Conclusion

Monte Carlo simulations used for the two new LDF prototypes validation showed results in accordance with the literature. For the non invasive prototype, the phantom model presented here, to evaluate the *in vitro* prototype response, has

shown good agreement with the theoretical expectations. M1 increases with the concentration and with the fibre distances. The mean depth increases with the fibre distance and decreases with the milk concentration. For the *in vivo* evaluation, the estimated parameters for the skin model corresponded to *a priori* expectations. We have shown that increasing the wavelength of the incoming light (in the range of 635-830 nm) increases the probed mean depth. Moreover, an increase of the source-detection fibre separations leads to a higher mean depth and M1, values. In what concerns the rat brain model, the mean depth that Doppler shifted photons travel was estimated to be 0.15 mm, which is in agreement with the literature.

4 - Non Invasive Prototype

4.1 Prototype Description

A new laser Doppler flowmeter prototype with depth discrimination capabilities is being built in order to discriminate between different microcirculatory skin layers. This prototype is a non-invasive and multi-wavelength device, with 635, 785, and 830 nm laser light wavelengths with a detection system using three optical fibres (enabling backscattered light detection at three different emitting-receiving fibre distances). The system has three constant power laser diodes drivers to supply the three laser diodes for 635, 785 and 830 nm wavelength. These laser drivers allow having a constant light power avoiding the fluctuations caused, for example, by temperature. The probe used to driving the laser light to the tissue and to collecting the skin backscattered light is from Perimed and has a central emitting fibre and collecting fibres located at 0.14, 0.25 and 1.2 mm from the emitting fibre. Three bi-cell photodetectors are used for backscattered light detection. The photocurrent in amplified and converted to voltage, it is digitalised by a data acquisition system from National Instruments® (NI-USB6212) and it is processed using Matlab software (Mathworks®).[17] The prototype has also a calibration system which provides the light intensity for the photodetectors calibration. This calibration system consists of three light emitting diodes (LEDs), with the three wavelengths used, with variable current sources. A microcontroller from Microchip, the PIC24FJ128GA010, gives us switching capabilities for the laser diodes and LEDs, current control and monitoring of the LEDs.[16]

4.2 *In vitro* validation

In vitro validation was performed in order to evaluate the performance of the prototype to different scatterers concentrations and velocities.

4.2.1 Methods

For *in vivo* validation two phantoms have been used. One consists of two glued acrylic plates with a 4×5 mm^2 excavated depression in one of them, used to study the linearity of the prototype in what concerns different scatterers velocity and

concentration. The other is the one used in Monte Carlo simulations and it possesses six layers of Teflon® microtubes (internal diameter of 0.25 mm and a external diameter of 0.76 mm) enabling signals depth discrimination. Milk was pumped through the depression in the acrylic phantom, or through the microtube, in the Teflon® phantom. As commercial skimmed milk has been chosen as a moving fluid, (mentioned in section 3.4.1) because it possesses suspension particles that act as scatterers. It has similar behaviour when compared with intralipid solutions and it is easier to handle and cheaper than blood.

The milk was pumped with a motorized syringe at 0, 0.5, 1.0, 1.5, 2.0, 2.5, 3.0, 3.5, 4.0, 4.5, 5.0, 5.5 and 6.0 mm/s in the acrylic phantom and at 1.56, 3.12, 4.68, 6.25, 7.78 and 9.35 mm/s in the Teflon® phantom. Measurements were taken with milk, and with two different aqueous milk solutions (50 % and 25 %). For each velocity and concentration the signal was sampled at 50 kHz, during ten minutes, with a Perimed probe positioned perpendicular to the surface of the phantom. The digitalised signal was then processed to give as output parameter the average perfusion (Perf) (see chapter 2). This procedure was applied to the three wavelengths.

The same protocol was executed with the commercial Periflux 5000 flowmeter, from Perimed, and with the prototype in order to compare the two flowmeters.[22]

4.2.2 Results and discussion

Several acquisitions have been done for each milk velocity and concentration. The summary of the results, as follows:

Periflux 5000 results

- ***Acrylic phantom results***

Previously it was stated that perfusion, Perf, is proportional to the concentration of the moving scatterers times its average velocity. The results obtained with the acrylic phantom are in agreement with this principle, as Perf increases with the velocity and with the concentration of the moving fluid for each emitting-receiving fibre distance as it can be observed in Fig. 12 a), b) and c). Moreover, was also noted that, increasing the emitting-receiving fibre distance, a larger Perf value is obtained, which is a result of the larger volume measured with larger emitting-receiving fibre separations as it can be seen in Fig. 12 d), e) and f). In figures 11 a), b), c) and f) one

can observe that, for the 1.2 mm emitting-collecting fibre distance perfusion saturates for the higher velocities. Moreover, it can be noticed that the velocity in which Perf saturates, decreases for higher milk concentrations. The device saturates, because it is constructed for blood flow measurements and milk does not have the same optical properties as blood. Furthermore, Perimed is for perfusion measurements in the living tissues and the phantom does not perfectly mimic them. Table 12 presents the statistics results of the linear regression study. The statistical analysis showed good correlation between the fitted model and the results since the coefficent of determination, R^2, is close to one and the p-value is lower than 0.01, i.e, there are 99% sure that there is a relationship between predictiors and the obtained values. Therefore, we can conclude that the relation between perfusion and velocity is linear, as expected.

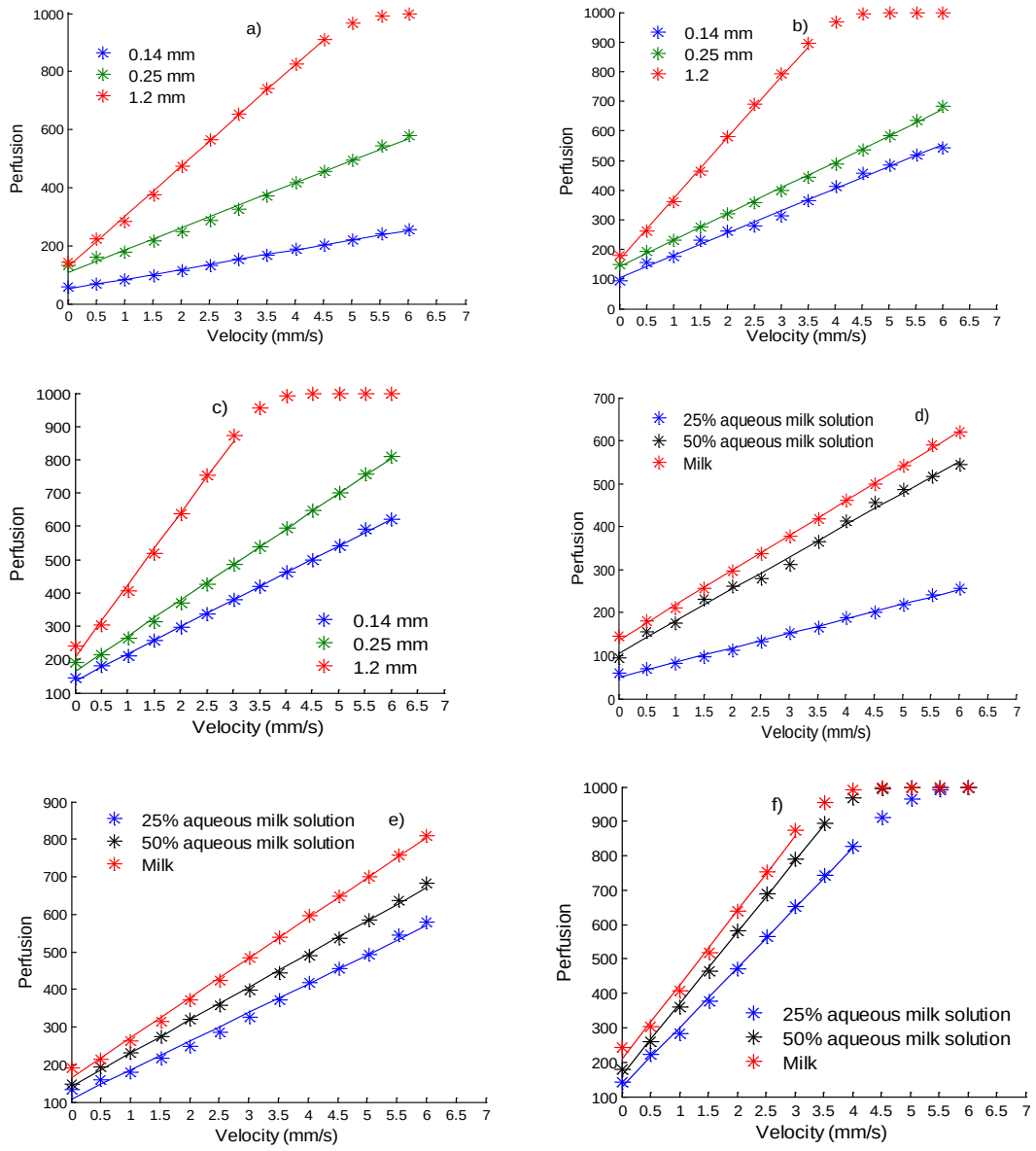

Figure 12: Perfusion vs. Velocity for: a) 25% ; b) 50% aqueous milk solutions and c) milk; and for: d) 0.14 mm; e) 0.25 mm and f) 1.2 mm emitting-receiving fibre distances. Results were taken using the acrylic phantom.

Table 12: Statistics of linear regression obtained in the acrylic phantom with Perimed. *m* and *b* are the one and zero degree polyminal coefficients, respectively, of the linear fitting. R^2 is the coefficient of determination and *p-value* is the significance of the F-statistic.

Milk concentration	Fibre distance	m	b	R^2	p-value
25%	0.14	33.83	50.15	1	<0.01
	0.25	76.74	107.9	0.99	<0.01
	1.2	173.35	127	1	<0.01
50%	0.14	74.41	106.04	0.99	<0.01
	0.25	88.16	141.79	1	<0.01
	1.2	193.32	180.84	1	<0.01
100%	0.14	80.8	136.12	1	<0.01
	0.25	106.55	164.22	1	<0.01
	1.2	187.58	243.43	0.99	<0.01

- ***Teflon® phantom results***

The results obtained with the Teflon® phantom are similar to the ones obtained with the acrylic phantom. Namely, the velocity of milk and the emitting-receiving fibre distance [c.f Fig 13 a), b) and c)], as Perf increases with these variables. Perfusion saturates for the 6.25 mm/s in milk using the 1.2 mm fibre separation. For the other emitting-receiving fibre distances perfusion never saturates, even for the maximum velocity 9.35 mm/s, in opposition to what happens in the acrylic phantom. Furthermore, checking figures 13 d), e) and f) it can be noticed that Perf also increase with the concentration of the moving fluid, except for the lower velocities using 0.14 and 0.25 fibre separations in the aqueous milk solutions. This might be due to the small inner diameter of the microtube that, together with the low velocities and low aqueous milk solutions, leads to the sub-estimation and uncertainties of the perfusion measurements. This may indicate that the phantom is more suitable for measuring larger sample volumes at higher milk solutions concentrations. The results of the linear regression analysis are presented in table 13, where it can be seen that R^2 is always close to one, i.e. that there is a good fitness between the linear model and the obtained results. It can also be seen that the p-values are always smaller than 0.01, except for the extreme circumstance of results collected with 1.2 mm fibre distance in milk. In this case it was only considered three samples for the regression analysis, so we cannot be confident, concerning the estimated values.

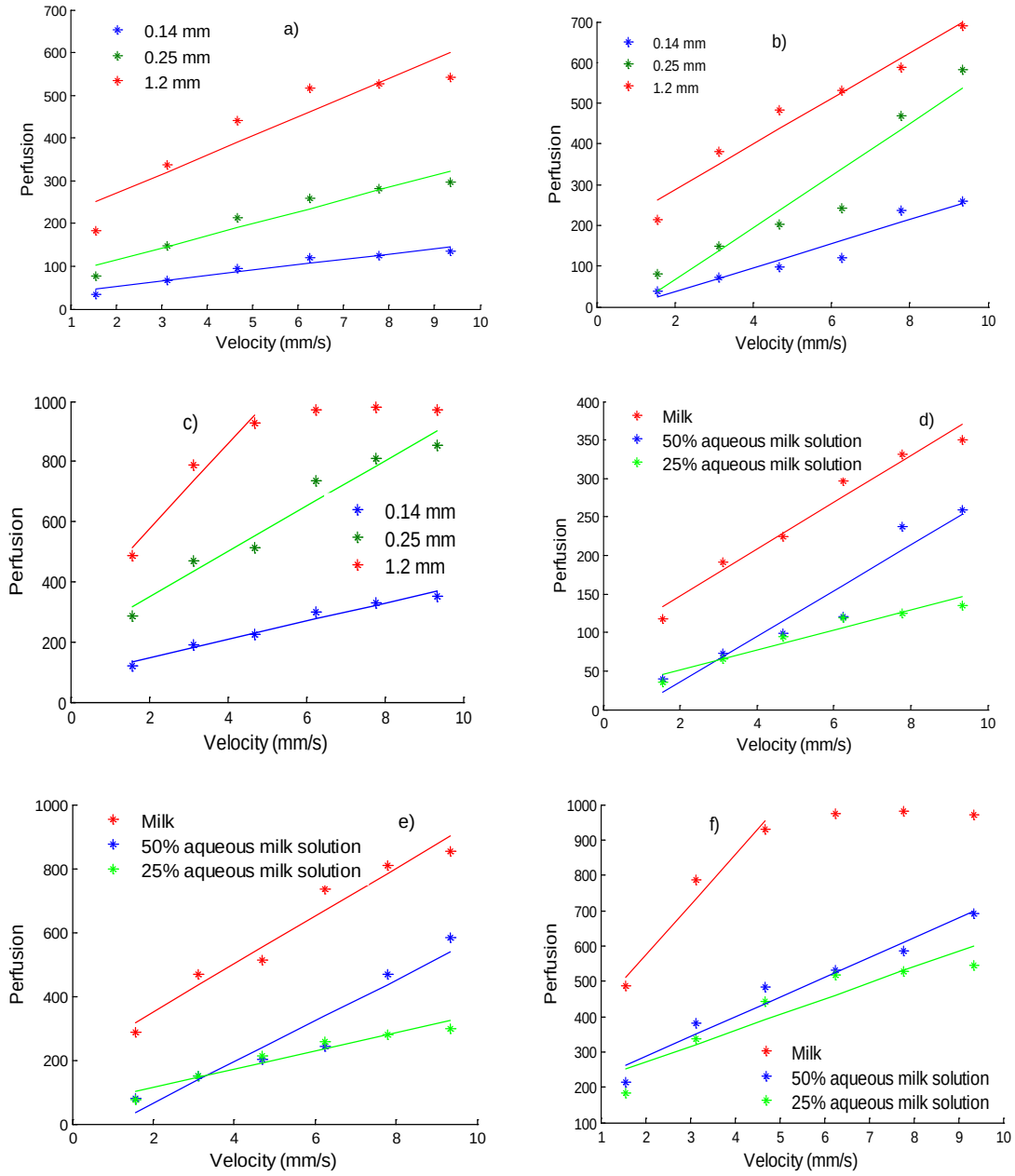

Figure 13: Perfusion vs. Velocity for: a) 25%; b) 50% aqueous milk solutions and c) milk; and for: d) 0.14 mm, e) 0.25 mm and for f) 1.2 mm emiting-receiving fibre distances. Results were taken using the Teflon® phantom, with Perimed.

Table 13: Statistics of linear regression obtained in the Teflon® phantom with Perimed. *m* and *b* are the one and zero degree polynomial coefficients, respectively, of the linear fitting. R^2 is the coefficient of determination and *p-value* is the significance of the F-statistic.

Milk concentration	Fibre distance	m	b	R^2	p-value
25%	0.14	30.35	86.28	0.97	<0.01
	0.25	74.98	201.53	0.96	<0.01
	1.2	141.9	291.1	0.96	0.13
50%	0.14	29.62	-23.4	0.92	<0.01
	0.25	64.22	63.3	0.92	<0.01
	1.2	55.9	175.79	0.96	<0.01
100%	0.14	12.87	25.8	0.93	<0.01
	0.25	28.4	57.49	0.94	<0.01
	1.2	44.93	180.09	0.86	<0.01

Prototype

- ***Acrylic phantom results***

In the acrylic phantom results obtained with the developed prototype, the Perf increases with milk velocity for all wavelengths of incoming light, as it was expected. Moreover, Perf also increases with the emitting-receiving fibre distance, which is in accordance with the theory that states that greater fibre distances leads to a larger sampled volume and consequently bigger values of Perf [cf. Fig. 14 a)]. Concerning the milk concentration, for 785 and 830 nm laser light wavelength the results are in agreement with theoretical expectations, i.e., Perf increases with the milk concentrations for each fibre distance and velocity. The same happens for 635 nm laser light for 0.14 fibre distance. Although for 635 nm for 0.25 and 1.2 fibre distance this does not happens. Instead, Perf decreases with the concentration (cf. Fig. 14 b)). The complete results are presented in appendix III. To investigate if the relationship between perfusion and milk velocity is linear, a linear fitting was performed (cf. tables 24, 25 and 26 in Appendix III). It can be seen that R^2 is never lower than 0.94 and the p-value is always lower than 0.01. Therefore, we can conclude that our perfusion measurements are linearly proportional to the velocity of the moving fluid.

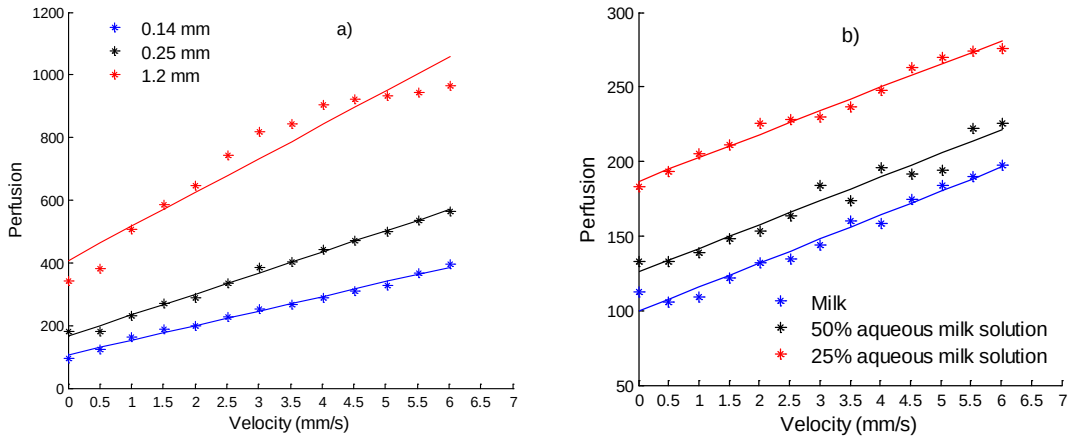

Figure 14: Perfusion vs. velocity for: a) 785 nm laser light and milk. b) 635 nm laser light and 0.25 mm source detector fibre distance.

Measurements with the depth discrimination Teflon® phantom were not yet made.

4.3 *In vivo* validation

The prototype is now being *in vivo* tested in healthy non-smoking participants.

4.3.1 Methods

The signal is being acquired in the forearm with the participants in the supine position and lasts, approximate, thirty three minutes. The measurements are being made in healthy, non-smoking, participants free of caffeine containing beverages in the measurements day. A reactive hyperaemia to arterial occlusion (PORH) test, using a pressure cuff placed around the upper limb, inflated for 3 min to 200 mmHg was used. Initially, resting baseline blood flux is recorded for 20 min, then the cuff is inflated for 3 min, finally, the cuff is deflated and then the returning to the baseline is recorded during 10 min.

For each subject, the protocol is repeated using the three lasers diodes existing in the prototype: 635, 785 and 830 nm, and also for the commercial flowmter, Periflux 5000 from Perimed, with the probe in the same position for the four measurements.

4.3.2 Preliminary results

The preliminary results are in accordance with the literature and with the commercial prototype results. In figure 15 it can be observed the obtained results for one participant using our prototype and the commercial flowmeter. Firstly, resting baseline blood flux is recorded for 20 min (T1). During the occlusion, perfusion

decreases for any fibre distance (T2). This was expected because the inflated pressure cuff placed around the upper limb decreases the blow flow, under the measurement area. After the occlusion, the reactive hyperaemia peak, p, occurs and then the signal returns to the baseline (T3). Comparing the results obtained with our prototype with the ones obtained from Periflux 5000 [cf. Fig. 15 d)], it can be noticed that both record the same alterations in Perf measurements.

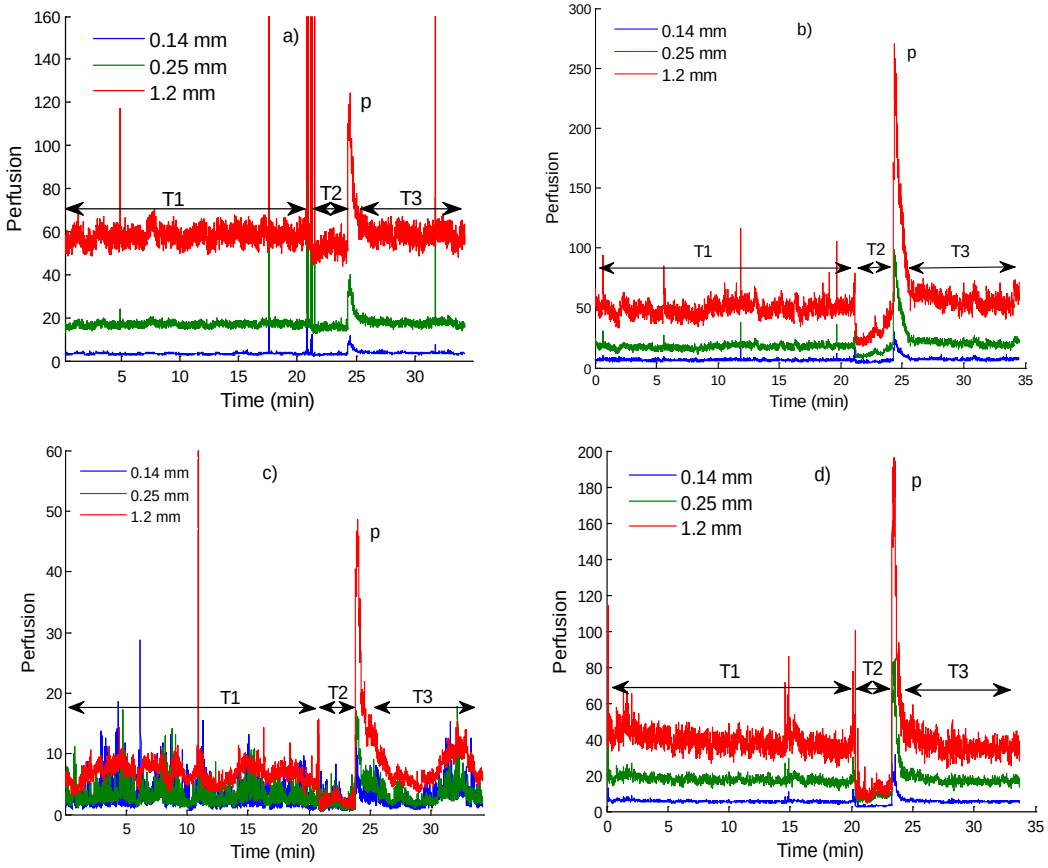

Figure 15: Signal collected in the human forearm with the non-invasive prototype with: a) 635; b) 785; c) 830 nm laser diode and d) with the commercial flowmeter.

4.4 Conclusions

In general, there are good agreement between the *in vitro* results of Periflux 5000 and our prototype taken on the acrylic phantom. In both systems Perf increases with the increasing of the parameters under evaluation, i.e, velocity, milk concentration and emitting-receiving fibre distance. There is only a mismatch with the theoretical expectations for the 635 nm laser diode in our prototype. Furthermore, it was statistically proved that Perf is linear proportional to the velocity of moving fluid, as theoretical principles indicate. Perfusion measurements taken on the Teflon®

phantom with the commercial prototype show that this phantom is suitable for depth measurements evaluation of our prototype.

In vivo preliminary results obtained with the non-invasive prototype are in accordance with the literature and with the commercial flowmeter.

5 - Invasive Prototype

5.1 Prototype Description

A self-mixing based prototype with a miniaturized laser Doppler probe is also being built in order to monitor blood flow changes in rat deep brain structures without causing significant damage to the brain tissue. In self-mixing method, the monitor photodiode of the laser diode is used for signal detection; a single optical fibre is therefore used for laser light emission and detection. Pigtailed laser diodes with single mode optical fibre are being used. The probe consists of the stripped optical fibre core inserted in a micro-needle with an outer diameter of 260 µm. As commercial available probes have a 450 µm diameter, the use of only one optical fibre allows us to reduce the size cross-section of the probe to 58%.

5.2 Software Interface

The prototype is now being *in vivo* tested. To make the acquisition simple and easy a graphical user interface (GUI) was created using the GUIDE tool, a MATLAB® graphical user interface development environment (cf. Fig 16). The developed GUI allows switching control of the laser diodes and real time signal processing. The signal processing consists in calculating the moments of the Doppler power spectrum with a frequency rate of 32Hz. Before starting an acquisition, the chosen laser diode is turned on, by the selection of the button 'Laser 785' or 'Laser 1300' for switching between 785 or 1300 nm laser diode, respectively. To start the acquisition the button 'Adquirir' must be pressed. The signal, sampled at 50Hz, will be displayed in the window a) of the GUI, and the processed signal in the window b). The panel c) allows registering events during the acquisition, such as administration of drugs, through the table A. The table can be saved by writing the name of the file on the box B and by selecting the button 'Guardar'. The button 'Tempo' present on panel c) informs how much time has passed since the beginning of the acquisition. The acquisition can be stopped by pressing the button ESC of the keyboard and the lasers can be switched off by pressing the button 'Desligar'.

This interface is being successfully used in the measurements.

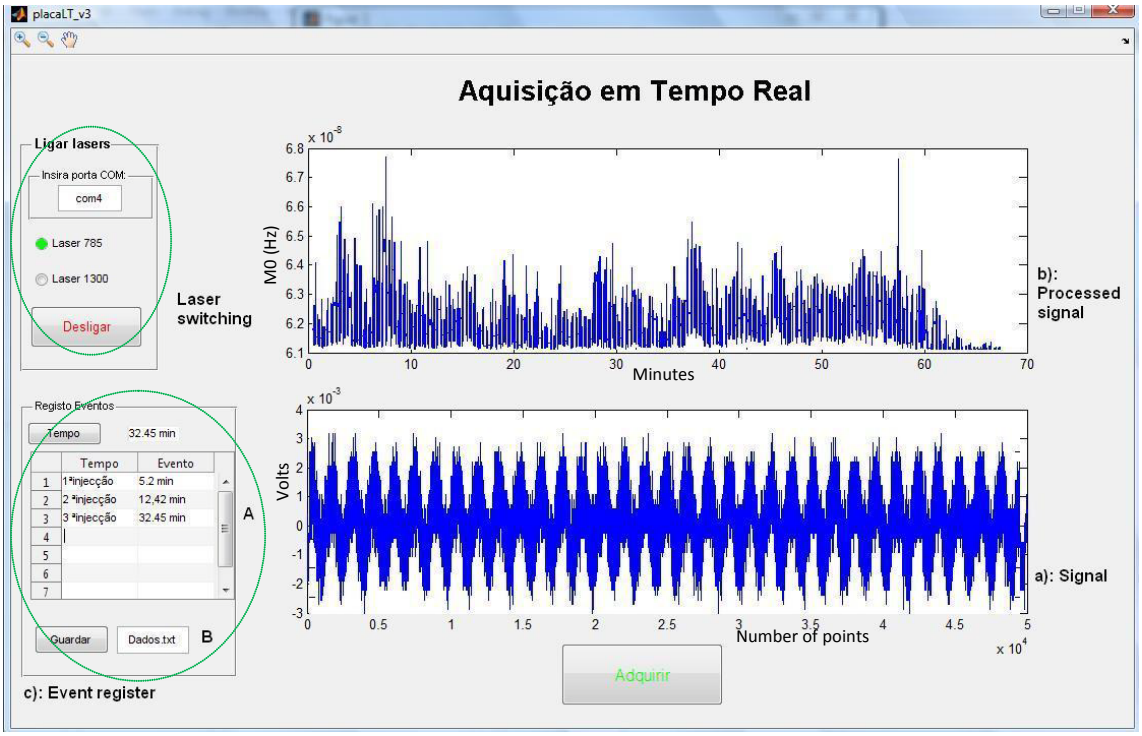

Figure 16: Graphical user interface developed for real time perfusion measurements in rat brain.

In Fig. 16) it can be observed in window b) the result obtained for a rat brain measurement. Zero order moment signal processing was used and it can be clearly seen that, after 60 minutes of measurements, the rat dies, because the signal oscillation decreases to near zero average amplitude.

6 - Final conclusions and Future work

6.1 Final conclusions

Monte Carlo simulations, applied to the new non-invasive LDF prototype validation, predicted that larger emitting-receiving fibre distances and higher wavelengths can measure blood perfusion in deep skin layers. This was also verified in the *in vitro* validation, i.e. higher values of perfusion were obtained with the higher wavelength and larger fibre distances. Moreover, the prototype has showed good response to the *in vitro* tests. *In vivo* preliminary results are in accordance with the literature and with the commercial flowmeter. Therefore, the results validate the prototype for microcirculation blood flow measurements on human skin and there are strong indicators that deep perfusion discrimination is possible using different wavelengths and emitting-receiving fibre distances.

The validation of the new invasive prototype for rat brain blood flow measurements is now being developed with the probe positioned 0.15 mm above the measurement area in rat brain, because it was predicted by Monte Carlo simulations that Doppler shifted photons will travel a mean depth of 0.15 mm, which is in agreement with the literature.

6.2 Future work

In vitro and *in vivo* validations conclusions, namely, measurements with the non-invasive prototype using the Teflon® phantom and statistical analysis, such as paired difference tests, on the *in vivo* results, to study the differences between perfusions collected with different laser diodes wavelengths and fibre distance, will be done.

Hardware improvements must be made, namely filtering the signal before sampling with an 8th order anti-aliasing filter, which will remove the noise peaks of the perfusion signals [cf. Fig. 15 a)].

Moreover, it is important to improve some aspects of the non invasive prototype, mainly in what concerns the signal processing system. The prototype does

not allow real time measurements as the signal processing is made *a posteriori* with the Matlab® software. Therefore, in order to improve this it is essential to incorporate on the prototype a digital signal processor (DSP).

In what concerns the invasive prototype, *in vivo* signal measurements and its analysis will be carried out, shortly. The results will be compared with the ones obtained with the commercial flowmeter, Periflux 5000, from Perimed.

Appendices

Appendix I – Phantom model-Monte Carlo simulations results

Table 14: The percentage of Doppler events detected, the mean of Doppler scattering events and the mean depth of the Doppler events for each photon for the phantom model (fibre distance and velocity pairs), with skimmed milk (100%).

Fibre distance (mm)	Velocity (mm/s)	Detected Doppler (%)	Mean Doppler scattering	Mean depth Doppler (mm)
0	1.56	10.27	10.08	0.32
	3.12	10.26	10.08	0.32
	4.68	10.19	10.24	0.32
	6.25	10.28	10.07	0.32
	7.78	10.27	10.09	0.32
	9.35	10.18	10.25	0.32
0.14	1.56	41.26	12.66	0.35
	3.12	41.28	12.68	0.35
	4.68	41.25	12.67	0.35
	6.25	41.25	12.65	0.35
	7.78	41.26	12.67	0.35
	9.35	41.27	12.68	0.35
0.25	1.56	56.45	14.27	0.37
	3.12	56.36	14.36	0.38
	4.68	56.48	14.27	0.37
	6.25	56.45	14.25	0.37
	7.78	56.37	14.37	0.38
	9.35	56.49	14.26	0.37
1.2	1.56	87.47	26.63	0.53
	3.12	87,5	26.51	0.53
	4.68	87.51	26.52	0.53
	6.25	87.48	26.56	0.53
	7.78	87.5	26.53	0.53
	9.35	87.52	26.53	0.53

Table 15: The percentage of Doppler events detected, the mean of Doppler scattering events and the mean depth of the Doppler events for each photon for the phantom model (fibre distance and velocity pairs), with aqueous milk solution (50%).

Fibre distance (mm)	Velocity (mm/s)	Detected Doppler (%)	Mean Doppler scattering	Mean depth Doppler (mm)
0	1.56	6.732	5.85	0.34
	3.12	6.697	5.97	0.34
	4.68	6.65	5.97	0.34
	6.25	6.73	5.87	0.34
	7.78	6.72	5.87	0.34
	9.35	6.64	5.96	0.34
0.14	1.56	32.35	7.3	0.39
	3.12	32.33	7.4	0.38
	4.68	32.33	7.41	0.39
	6.25	32.18	7.32	0.38
	7.78	32.14	7.32	0.38
	9.35	32.3	7.42	0.39
0.25	1.56	47.76	7.78	0.4
	3.12	48.08	7.78	0.41
	4.68	48.09	7.78	0.41
	6.25	47.72	7.79	0.41
	7.78	48.05	7.78	0.41
	9.35	47.94	7.77	0.41
1.2	1.56	86	12.65	0.55
	3.12	85.82	12.6	0.54
	4.68	85.98	12.6	0.55
	6.25	85.82	12.61	0.54
	7.78	86.02	12.62	0.55
	9.35	85.99	12.64	0.55

Table 16: The percentage of Doppler events detected, the mean of Doppler scattering events and the mean depth of the Doppler events for each photon for the phantom model (fibre distance and velocity pairs), with aqueous milk solution (25%).

Fibre distance (mm)	Velocity (mm/s)	Detected Doppler (%)	Mean Doppler scattering	Mean depth Doppler (mm)
0	1.56	4.77	3.48	0.36
	3.12	4.76	3.46	0.36
	4.68	4.8	3.47	0.36
	6.25	4.78	3.47	0.36
	7.78	4.9	3.5	0.36
	9.35	4.9	3.37	0.36
0.14	1.56	26	4.29	0.41
	3.12	25.86	4.29	0.41
	4.68	25.6	4.29	0.41
	6.25	26.1	4.26	0.41
	7.78	26.1	4.25	0.41
	9.35	26.1	4.26	0.41
0.25	1.56	82	4.37	0.56
	3.12	82	4.37	0.55
	4.68	82	4.37	0.56
	6.25	81.9	4.4	0.56
	7.78	81.9	4.4	0.56
	9.35	81.8	4.4	0.56
1.2	1.56	82	6.47	0.56
	3.12	82	6.49	0.55
	4.68	82	6.49	0.56
	6.25	81.9	6.46	0.56
	7.78	81.9	6.46	0.56
	9.35	81.8	6.46	0.56

Table 17: First moment of Doppler power spectrum (M1) obtained in the phantom model (fibre distance and velocity pairs), with milk (100%).

Fibre distance (mm)	Velocity (mm/s)	M1
0	1.56	1.79E+20
	3.12	3.55E+20
	4.68	4.93E+20
	6.25	6.13E+20
	7.78	6.54E+20
	9.35	6.71E+20
0.14	1.56	7.08E+20
	3.12	1.39E+21
	4.68	1.95E+21
	6.25	2.28E+21
	7.78	2.41E+21
	9.35	2.45E+21
0.25	1.56	9.68E+20
	3.12	1.87E+21
	4.68	2.58E+21
	6.25	2.99E+21
	7.78	3.11E+21
	9.35	3.13E+21
1.2	1.56	1.87E+21
	3.12	3.29E+21
	4.68	4.05E+21
	6.25	4.20E+21
	7.78	4.06E+21
	9.35	3.78E+21

Table 18: First moment of Doppler power spectrum (M1) obtained in the phantom model (fibre distance and velocity pairs), with aqueous milk solution (50%).

Fibre distance (mm)	Velocity (mm/s)	M1
0	1.56	1.09E+20
	3.12	2.16E+20
	4.68	3.13E+20
	6.25	3.77E+20
	7.78	4.13E+20
	9.35	4.18E+20
0.14	1.56	5.35E+20
	3.12	1.01E+21
	4.68	1.44E+21
	6.25	1.70E+21
	7.78	1.85E+21
	9.35	1.91E+21
0.25	1.56	7.65E+20
	3.12	1.44E+21
	4.68	2.02E+21
	6.25	2.38E+21
	7.78	2.55E+21
	9.35	2.61E+21
1.2	1.56	1.51E+21
	3.12	3.70E+21
	4.68	3.53E+21
	6.25	3.89E+21
	7.78	3.94E+21
	9.35	3.80E+21

Table 19: First moment of Doppler power spectrum (M1) obtained in the phantom model (fibre distance and velocity pairs), with aqueous milk solution (25%).

Fibre distance (mm)	Velocity (mm/s)	M1
0	1.56	6.26E+19
	3.12	1.20E+20
	4.68	1.76E+20
	6.25	2.21E+20
	7.78	2.56E+20
	9.35	2.72E+20
0.14	1.56	3.52E+20
	3.12	6.75E+20
	4.68	9.74E+20
	6.25	1.18E+21
	7.78	1.31E+21
	9.35	1.39E+21
0.25	1.56	5.20E+20
	3.12	9.90E+20
	4.68	1.43E+21
	6.25	1.74E+21
	7.78	1.92E+21
	9.35	2.03E+21
1.2	1.56	1.10E+21
	3.12	2.02E+21
	4.68	2.77E+21
	6.25	3.23E+04
	7.78	3.44E+21
	9.35	3.54E+21

Table 20**:** The average path number, the average path depth and the mean path length for photon for the phantom model using a 25% aqueous milk solution.

Velocity (mm/s)	Fibre distance (mm)	Paths number	<path depth> (mm)	<path length> (mm)
1.56	0	3.31	1.45	10.66
	0.14	7.00	0.23	2.53
	0.25	9.66	0.23	2.55
	1.2	25.67	0.47	5.95
3.12	0	3.31	1.45	10.69
	0.14	7.00	0.23	2.53
	0.25	9.67	0.23	2.55
	1.2	25.72	0.47	5.95
4.68	0	3.31	1.45	10.61
	0.14	7.00	0.23	2.53
	0.25	9.68	0.23	2.53
	1.2	25.72	0.47	5.95
6.25	0	3.31	1.45	10.63
	0.14	6.97	0.23	2.53
	0.25	9.70	0.23	2.53
	1.2	25.66	0.47	5.95
7.78	0	3.33	1.43	10.69
	0.14	6.97	0.23	2.53
	0.25	9.68	0.23	2.55
	1.2	25.67	0.47	5.94
9.35	0	3.32	1.44	10.69
	0.14	6.99	0.23	2.53
	0.25	9.69	0.23	2.53
	1.2	25.66	0.47	5.95

Table 21: The average path number, the average path depth and the mean path length for photon for the phantom model, using a 50% aqueous milk solution.

Velocity (mm/s)	Fibre distance (mm)	Paths number	<path depth> (mm)	<path length> (mm)
1.56	0	3.37	1.41	10.74
	0.14	7.06	0.24	2.58
	0.25	9.51	0.22	2.45
	1.2	25.91	0.47	6.07
3.12	0	3.38	1.40	10.80
	0.14	7.04	0.24	2.58
	0.25	9.64	0.23	2.47
	1.2	26.09	0.46	6.01
4.68	0	3.38	1.43	10.80
	0.14	7.04	0.24	2.59
	0.25	9.61	0.22	2.46
	1.2	26.28	0.47	6.07
6.25	0	3.37	1.41	10.74
	0.14	6.98	0.23	2.49
	0.25	9.51	0.22	2.45
	1.2	26.10	0.46	6.01
7.78	0	3.37	1.41	10.73
	0.14	6.98	0.23	2.48
	0.25	9.61	0.23	2.46
	1.2	26.25	0.47	6.07
9.35	0	3.38	1.43	10.80
	0.14	7.0515	0.24	2.59
	0.25	9.54	0.22	2.50
	1.2	26.27	0.47	6.07

Table 22: The average path number, the average path depth and the mean path length for photon for the phantom model, using milk.

Velocity (mm/s)	Fibre distance (mm)	Paths number	<path depth> (mm)	<path length> (mm)
1.56	0	3.49	1.41	10.43
	0.14	7.04	0.22	2.53
	0.25	9.53	0.21	2.43
	1.2	27.67	0.45	6.24
3.12	0	3.49	1.41	10.43
	0.14	7.05	0.22	2.53
	0.25	9.54	0.21	2.45
	1.2	27.59	0.45	6.23
4.68	0	3.51	1.39	10.36
	0.14	7.04	0.22	2.52
	0.25	9.54	0.22	2.44
	1.2	27.59	0.45	6.22
6.25	0	3.49	1.41	10.43
	0.14	7.04	0.22	2.52
	0.25	9.52	0.21	2.42
	1.2	27.62	0.45	6.23
7.78	0	3.49	1.40	10.43
	0.14	7.04	0.22	2.53
	0.25	9.55	0.22	2.46
	1.2	27.61	0.45	6.23
9.35	0	3.51	1.39	10.36
	0.14	7.05	0.22	2.53
	0.25	9.53	0.21	2.43
	1.2	27.62	0.45	6.23

Appendix II – Mesurements depth results of Fredriksson *et al* [19]

Table 23: Measurements depth for skin model obtained by Fredriksson *et al.* [19] Table adapted from table 9 from Fredriksson *et al*.[19]

Wavelength (nm)	Fibre distance (mm)	Measurement depth (mm)
633	0	0.3
	0.25	0.32
	0.5	0.34
	1.2	0.4
780	0	0.32
	0.25	0.35
	0.5	0.37
	1.2	0.58

Appendix III – *In vitro* results of the prototype

- ***Light source 635 nm***

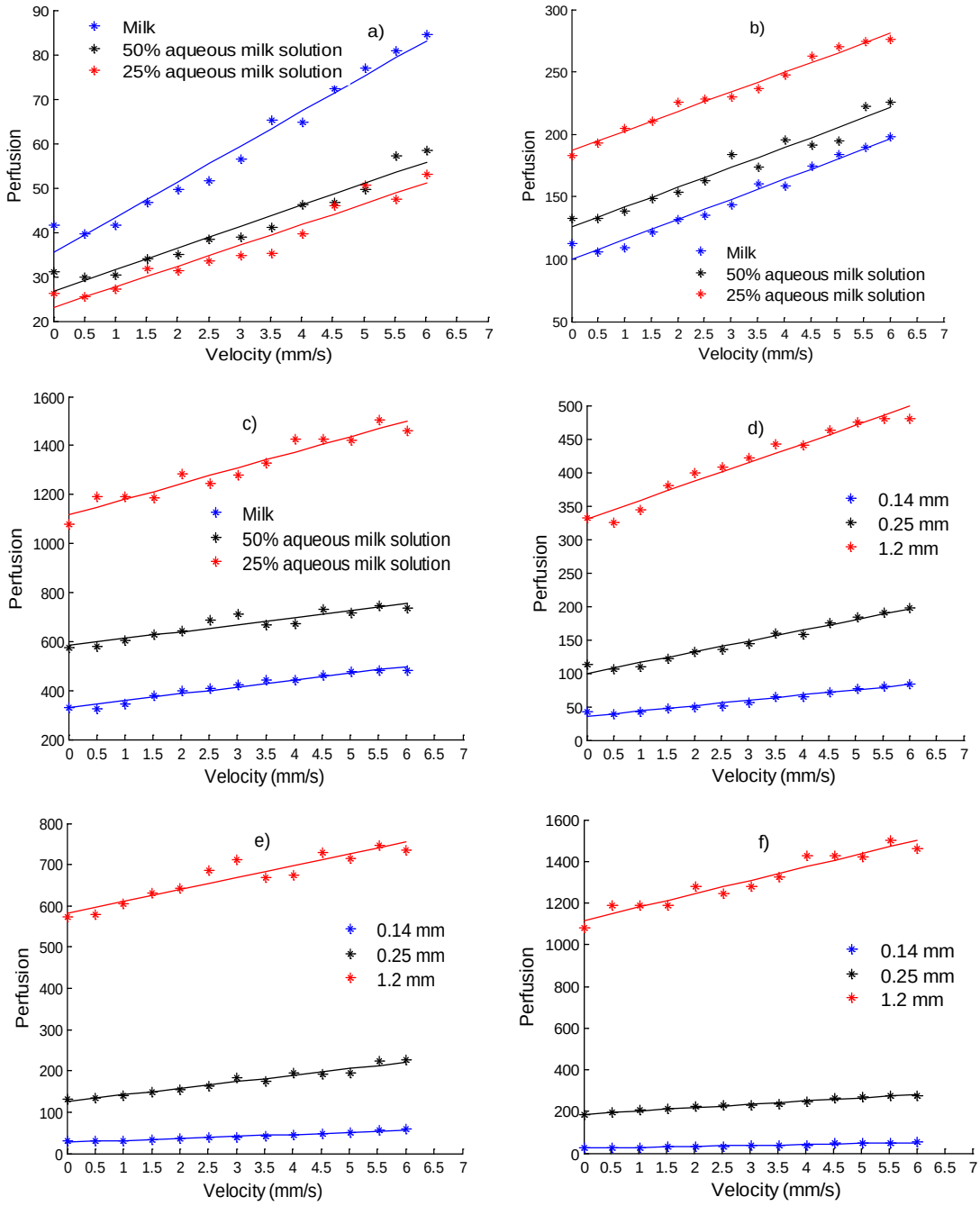

Figure 17: Perfusion vs. Velocity for: a) 0.14 mm, b) 0.25 mm and c) 1.2 mm emitting-receiving fibre distance. Perfusion vs. Velocity for: d) milk, e) 50% and f) 25% of milk concentration for signals collected using 635 nm laser light source.

Table 24: Statistics of linear regression obtained in the acrylic phantom with 635 nm laser light source. *m* and *b* are the polynomial coefficients (one and zero degree, respectively) of the linear fitting. R^2 is the coefficient of determination and *p-value* is the significance of the F-statistic.

Fibre distance (mm)	Milk concentration	m	b	R^2	p-value
0.14	100%	7.94	35.43	0.97	<0.01
	50%	4.83	26.74	0.94	<0.01
	25%	4.65	23.07	0.94	<0.01
0.25	100%	16.08	99.59	0.97	<0.01
	50%	15.90	125.70	0.95	<0.01
	25%	15.67	186.84	0.98	<0.01
1.20	100%	27.94	330.45	0.96	<0.01
	50%	28.49	583.11	0.88	<0.01
	25%	64.13	1115.95	0.93	<0.01

- ***Light source 785 nm***

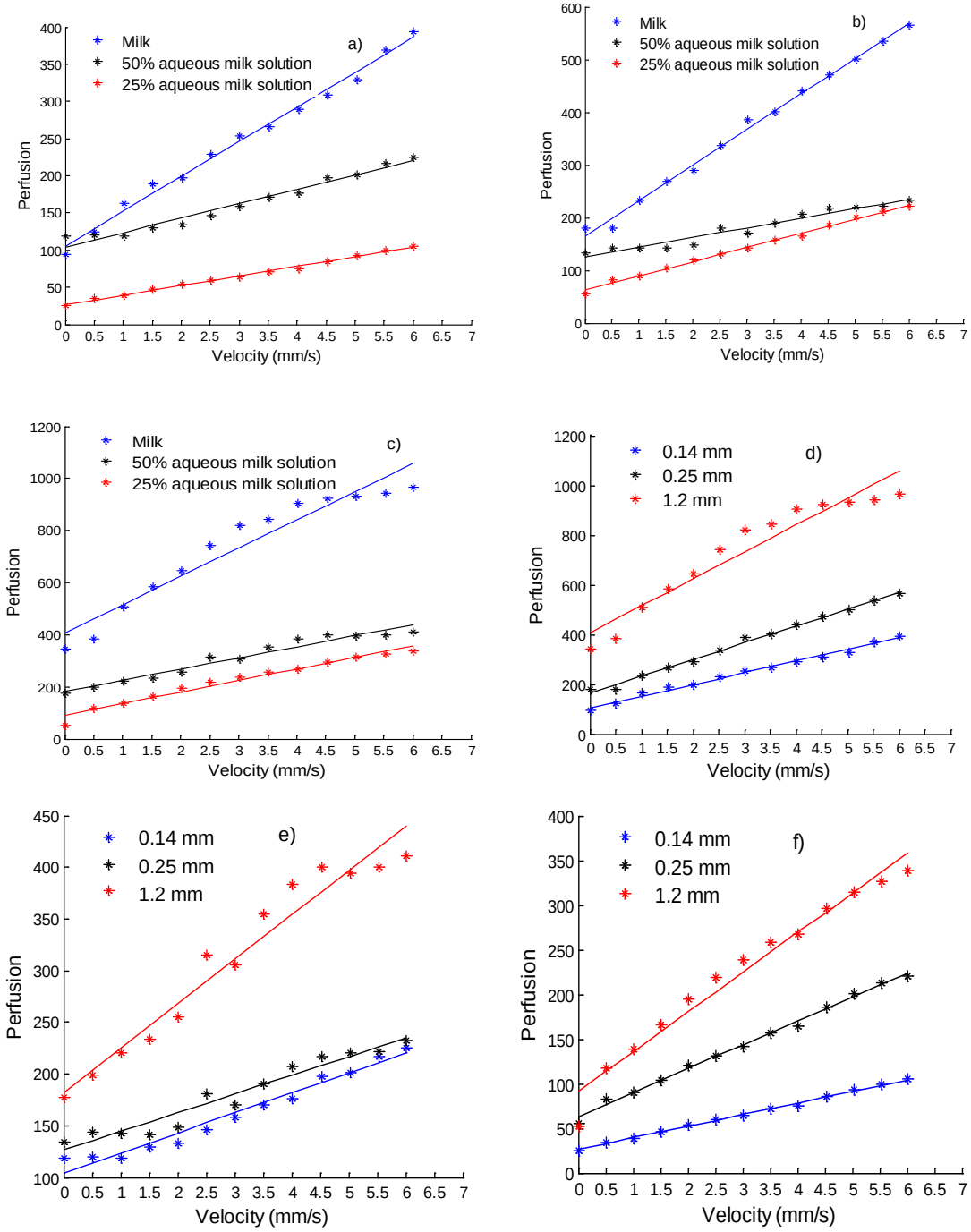

Figure 18: Perfusion vs. Velocity for: a) 0.14 mm, b) 0.25 mm and c) for 1.2 mm emitting-receiving fibre distance. Perfusion vs. Velocity for: a) milk, b) 50% and c) 25% of milk concentration for signals collected with 785 nm laser light.

Table 25: Statistics of linear regression obtained in the acrylic phantom with 785 nm laser light source. m and b are the polynomial coefficients (one and zero degree, respectively) of the linear fitting. R^2 is the coefficient of determination and p-value is the significance of the F-statistic.

Fibre distance (mm)	Milk concentration	m	b	R^2	p
0.14	100%	48.71	108.96	0.92	<0.01
	50%	19.22	61.75	0.95	<0.01
	25%	13.00	44.68	0.81	<0.01
0.25	100%	99.91	197.46	0.95	<0.01
	50%	72.08	180.73	0.99	<0.01
	25%	55.85	113.14	0.90	<0.01
1.20	100%	169.92	320.44	0.94	<0.01
	50%	118.43	191.09	0.98	<0.01
	25%	70.84	111.90	0.94	<0.01

- *Light source 830 nm*

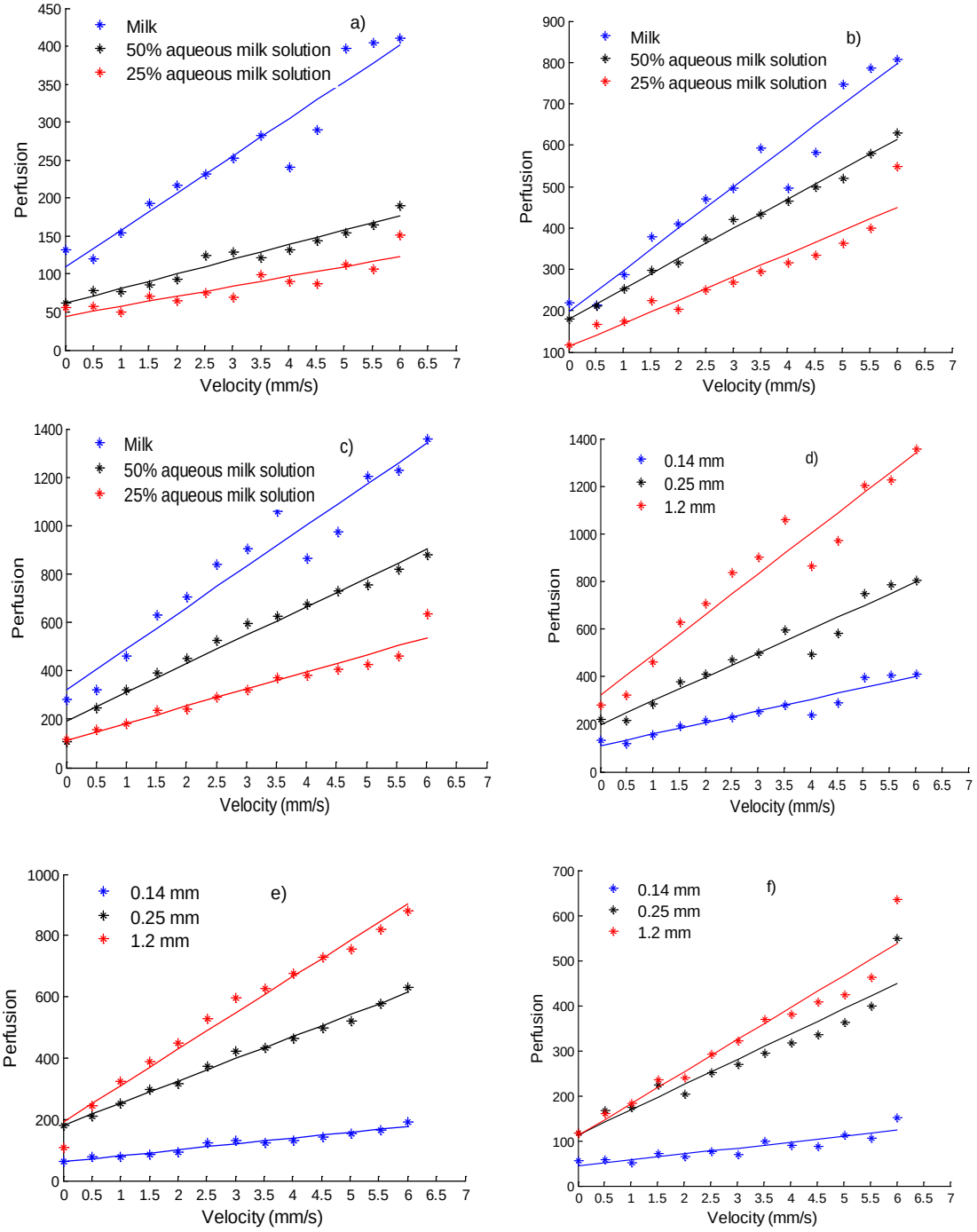

Figure 4: Perfusion vs. Velocity for: a) 0.14 mm, b) 0.25 mm and c) 1.2 mm emiting-receiving fibre distance. Perfusion vs. Velocity for: a) milk, b) 50% and c) 25% of milk concentration for signals collected with 830 nm laser light sorce.

Table 26: Statistics of linear regression obtained in the acrylic phantom with 830 nm laser light. *m* and *b* are the polynomial coefficients (one and zero degree, respectively) of the linear fitting. R^2 is the coefficient of determination and *p-value* is the significance of the F-statistic.

Fibre distance (mm)	Milk concentration	m	b	R^2	p-value
0.14	100%	46.76	105.67	0.99	<0.01
	50%	19.34	104.18	0.97	<0.01
	25%	12.98	26.41	1.00	<0.01
0.25	100%	67.19	165.71	0.99	<0.01
	50%	18.06	126.39	0.95	<0.01
	25%	26.74	63.17	0.99	<0.01
1.20	100%	108.03	407.97	0.93	<0.01
	50%	42.83	182.41	0.95	<0.01
	25%	44.38	91.35	0.97	<0.01

References

[1] I. Fredriksson, C. Fors, and J. Johansson. Laser doppler Flowmetry - a theoretical framework, 2007.

[2] F. Morales. Improving the clinical applicability of laser Doppler perfusion monitoring. PhD thesis, Groningen University , 1975.

[3] I. Fredriksson. Quantitative laser Doppler Flowmetry. Dissertation, Linkoping university, 2009

[4] P.A. Shepherd and P.A.Öberg. Laser-Doppler blood Flowmetry, chapter 2. Kluwer academic publishers, 1990

[5] A. K. Murray, A. L. Herrick and T. A. King. Laser Doppler imaging: a developing technique for application in the rheumatic diseases. Rheumatology, 43:1210-1218, 2004

[6] N. Vongsavan and B.Matthews. Some aspects of the use of laser Doppler flowmeters for recording tissue blood flow.Experimental physiology, 78:1-14, 1993.

[7] D. P. Kernick, J. E. Tooke and A. C. Shore. The biological zero signal in laser fluximetry – origins and practical implications. Eur J Physiol, 437:624-631,1999

[8] G. E. Nilsson, E. G. Salerud, N. O.T. Stromberg, and K. Wardell. Biomedical Photonics handbook, chapter 15. CRC press, 2003.

[9] J. H. Barker and T. J. Ryan. Clinically applied microcirculation research, chapter 24. CRC press, 1995

[10] L. A. Holowatz, C. S. Thompson-Torgerson and W. L. Kenney. The human Cutaneous circulation as a model of generalized microvascular function. J Appl Physiol, 105:370-372, 2008.

[11] E. Berardesca, J. L. Lévêque and P. Masson. EEMCO Guidance for the meaasurement of skin microcirculation, skin pharmacol. Appl. Skin Physiol, 15:442-456

[12] R. F. S. Gomes. Optimizaçao da focagem de feixes laser em tecidos biológicos: Desenvolvimentos de um simulador ópticos. Dissertation, Universidade Nova de Lisboa, 2011.

[13] M. Hülsbusch, D. Hölscher and V. Blazer. Spectral Monte-Carlo simulations of photon penetration biotissue in visible and near infrared. Progress in electromagnetic research symposium, Prague, 2007.

[14] E. Figueiras, L. F. F. Requicha, F. F. M. De Mul, and A. Humeau. Numerical simulation – Applications, examples and theory, chapter 7. InTech, 2007

[15] F. F. M. De Mul. Monte-Carlo simulation of Light transport in Turbid Media. Kluwer Publishers, 2004.

[16] O. Ricardo, S. Semedo, E. Figueiras, L. F. Requicha. Laser Doppler flowmeters for microcirculation measurements. 1st Portuguese meeting in Bioengineering, Technical University of Lisbon, 2011

[17] I. Fredriksson, M. Larsson and T. Strömberg. Optical microcirculatory skin model: assessed by Monte Carlo simulations paired with in vivo laser Doppler Flowmetry. Journal of Biomedical Optics, 13:014015, 2008.

[18] I. Fredriksson, M.Larsson and T. Strömberg. Measurement depth and volume in laser Doppler Flowmetry. Microvascular research, 78:4-13, 2009.

[19] J. Mobley and T. Vo-Dinh. Biomedical Photonics handbook, chapter 2. CRC press, 2003

[20] D. W. Hahm. Light Scattering Theory. Department of mechanical and Aerospace Engineering, University of Florida, 2009.

[21] http://www.perimed-instruments.com/, acess in 20 July 2011

[22] E. Figueiras, L.F.R. Ferreira, and A. Humeau. Phantom validation for depth assessment in laser Doppler flowmetry technique. Proceedings of EOS, Topical Meeting on Diffractive Optics, 2413, Koli, 2010

[23] F. F. M. de Mul, M. H. Koelink, M. L. Kok, P. J. Harmsma, J. Greve, R. Graaff and J.G. Aarnoudse. Laser Doppler Velocimetry and Monte Carlo Simulations on Models for Blood Perfusion in Tissue. Applied Optics, 34:6595-6611, 1995.

[24] F. F. M. De Mul. Monte-Carlo simulation of Light transport in Turbid Media, Chapter 12. In: Handbook of Coherent Domain Optical Methods, Biomedical Diagnostics, Environment and Material Science, Kluwer Publishers, 2004.

[25] M. D. Waterworth, b. J. Tarte, A. J. Joblin, T. van Doorn, and H. E. Niesler .Optical transmission properties of homogenized milk used as a phantom material in visible wavelength imaging. Australasian Physical and Engineering Sciences in Medicine, 18:39-44, 1995.

[26] Q. Li, B. J. Lee, Z. M. Zhang and D. W. Allen. Light scattering of semitransparent sintered polytetrafluoroethylene films. Journal of Biomedical Optic, 13(5):054064, 2008.

[27] C. R. Simpson, M. Kohl, M. Essenpreis and M. Cope. Near infrared optical properties of ex-vivo human skin and subcutaneous tissues measured using the Monte Carlo inversion technique. Phys Med Biol, 43:2465-2478, 1998

[28] Prahl. Optical Absorption of Hemoglobin, 1999. Retrived from http://omlc.ogi.edu/spectra/hemoglobin/index.html

[29] L. M. Hamberg, G. J. Hunter, D. Kierstead, E. H. Lo, R. G. Gonzalez and G. I. Wolf. Measurement of cerebral blood volume with substraction three-dimentional functional CT. Am. J. Neuroradiol, 17(10):1861-1869, 1996.

[30] H. C. van de Hulst. Light scattering by small particles. Dover publications, 1957,1981.

[31] C. Riva, B. Ross and GB. Benedeck. Laser Doppler measurements of blood flow in cappilary tubes and retinal arteries. Invest ophthalmol, 11(11) :936-944, 1972.

[32] M. D. Stern. In vivo evaluation of microcirculation by coherent light scattering. Nature, 254(5495):56-58, 1975.

[33] A. Liebert, M. Leahy, R. Maniewski. Multichannel laser-Doppler probe for blood perfusion measurements with depth discrimination. Med. Biol. Eng. Comput., 36 :740-747, 1998.

[34] E. Figueiras, V. Loureiro, L.F. Requicha Ferreira and A. Humeau. Some reasons to built a new laser Doppler flowmeter to monitor microvascular blood flow. IFMBE Proceedings, Medical Physics and Biomedical Engineering World Congress 2009; 25\IV:1865-1868, Munich, 2009.

[35] A. T. Forrester. Photoelectric mixing as a spectroscopic tool. Journal of the optical society of America. 51(3):253-259, 1961

[36] H. Z. Cummins, H. L. Swinney. Light beating spectroscopic, pp 135-200. In: Progress in optics, Wolf E. (ed), Amestardam, 1970.

[37] M. Larsson. Influence of optical properties on laser Doppler Flowmetry. Linköping university, 2004.